Thesis for the degree
Master of Science

Submitted to the Scientific Council of the
Weizmann Institute of Science
Rehovot, Israel

עבודת גמר (תזה) לתואר
מוסמך למדעים

מוגשת למועצה המדעית של
מכון ויצמן למדע
רחובות, ישראל

By
Tom Shahaf

מאת
תום שחף

הזרקת לייזר וביטול רעשים בסיב אופטי לשליטה מדויקת בקיוביטים

Laser Injection Lock and Fiber Noise Cancellation for Qubit control

Advisor:
Ziv Meir

מנחה:
זיו מאיר

Month and Year
July 2025

חודש ושנה עבריים
תמוז תשפ"ה

Abstract

We built and characterized a laser stabilization scheme tailored for precision control of a trapped-ion qubit. A high-power diode laser is injection-locked to a remote stable 729 nm master laser, with fiber noise cancellation (FNC) applied on the 120 fiber link connecting them—actively stabilizing the phase of the light before amplification. This configuration suppresses fiber-induced phase noise prior to injection locking, allowing narrow-linewidth, low-noise light to seed the slave laser.

We characterize the stabilized system using out-of-loop measurements of the beta-separation line and in-loop phase stability diagnostics, confirming high phase coherence and wavelength stability. By thoroughly exploring the injection parameter space of the slave diode, we obtain a detailed understanding of the master–slave configuration.

We demonstrate the viability of the system through high-resolution spectroscopy on a single trapped Ca^+ ion. Sideband-resolved spectra confirm operation in the Lamb–Dicke regime, and spectroscopy measurements indicate improved short-term stability. The observed spectral features and robust ion–laser coherence validate the system's performance for quantum control.

This architecture—integrating injection locking with FNC—provides a reliable platform for coherent spectroscopy and quantum logic operations.

Acknowledgements

This thesis is the product of two years of work, and the journey extended far beyond the original timeline. There's a saying: "If you want to go fast, go alone. If you want to go far, go together." This thesis is a clear case of the latter.

I would like to thank the many people who made this work possible. Meir Alon built the fiber noise cancellation phase-locked loop (FNC PLL), which was central to the project. Dr. Nitzan Akerman generously provided the clock laser and was always available for advice, feedback, and technical discussions throughout every stage of this work.

I am grateful to all my lab mates-Mai Faibish, Noga Saban, Evgenii Kipiatkov, Yonatan Schweitzer, Dror Einav, Idan Hochner, and Orr Barnea-for creating a warm, collaborative, and motivating working environment. In particular, I would like to thank Dror, Idan, and Orr for building the trapping and cooling apparatus and for their generous help in resolving many technical issues. Our discussions often sparked new ideas and helped move the project forward.

I owe special thanks to my advisor, Dr. Ziv Meir, for being deeply involved, encouraging, and genuinely invested in both the project and my development as a scientist. It is rare and incredibly rewarding to have such engaged mentorship.

Finally, I thank my wife, Gal, for smiling politely through explanations that even I wasn't sure I understood.

To everyone who walked this path with me-thank you.

Contents

List of Abbreviations

Δ Laser detuning from resonance

η Lamb–Dicke parameter

γ Full Width at Half Maximum (FWHM) linewidth

λ Wavelength of light

μ_B Bohr magneton

Ω Rabi frequency

$^{2S+1}L_J$ Spectroscopic term symbol: S is the total spin, L the orbital angular momentum, and J the total angular momentum

g_J Landé g-factor

m_J Magnetic quantum number (projection of J)

AOM Acousto-Optic Modulator

FNC Fiber Noise Cancellation

PID Proportional–Integral–Derivative (controller)

PMT Photomultiplier Tube

PSD Power Spectral Density

RF Radio Frequency

1 Introduction

The ability to control and measure quantum systems with high precision lies at the foundation of many of the most powerful technologies and profound scientific discoveries of the 21st century. From the definition of time and the operation of GPS networks to the rise of quantum computing and tests of fundamental symmetries, the tools of atomic, molecular, and optical (AMO) physics have redefined what is experimentally possible [1–4].

Central to this revolution is the laser [5]-an instrument that provides coherent, tunable, and highly controllable light across a vast range of wavelengths. Precision in AMO physics depends critically on the stability and coherence of laser light. Whether probing optical clock transitions at sub-Hz linewidths [6, 7] or performing quantum-logic gates with trapped ions [8], the demands on laser systems are constantly increasing.

Ultra-stable optical clocks based on ions such as $^{27}Al^+$ [9] or neutral atoms in optical lattices like ^{87}Sr [10] require lasers with linewidths well below one hertz, typically stabilized using high-finesse Fabry-Pérot cavities and frequency combs [9]. Other systems employ Doppler-free saturated absorption [11], electromagnetically induced transparency (EIT) [12], or offset locks to reference lasers or atomic lines [13]. Laser stabilization is equally critical in quantum computing platforms. Trapped ions, neutral atoms, superconducting circuits with optical interfaces, and even photonic qubits all rely on lasers for coherent control, measurement, and clocking.

In trapped-ion systems, lasers enable sideband cooling, spin-motion entanglement, and high-fidelity gate operations [14]-all of which depend on laser linewidth, intensity stability, and phase coherence. As an example, the electric quadrupole transition in $^{40}Ca^+$ at 729 nm offers an accessible, narrow-line testbed with a natural linewidth of 0.14 Hz, ideal for benchmarking laser performance. Within this broader context, our work focuses on developing a stable 729 nm laser system suitable for coherent control of a single trapped $^{40}Ca^+$ ion. The aim is not to match the ultimate performance of clock lasers, stabilized to cryogenic reference cavities [6, 7], but to create a robust, modular, and scalable system capable of narrow-linewidth operation with good phase stability across a laboratory-scale experimental setup. This system is designed to support quantum control experiments today and to serve as a foundation for molecular-ion spectroscopy [15, 16] and high-precision tests of fundamental physics in the near future [17].

Rather than develop an independent cavity- or comb-stabilized system, we use a master-slave laser configuration in which the master laser-already stabilized to a high-finesse cavity in a separate laboratory-seeds a high-power slave diode via optical injection locking [18]. This approach allows us to inherit the narrow linewidth and spectral purity of the master while retaining flexibility in optical routing and power distribution. Injection locking, in this context, acts as a passive coherence transfer technique, enabling us to replicate the stable light in our own experimental zone without the need for additional frequency-locking electronics. Although not fully autonomous, this approach provides a reliable and scalable solution for numerous precision tasks, especially in a setting where the laser serves as a shared frequency reference for other stabilized systems.

A critical challenge in delivering phase-stable light to a remote quantum system is the accumulation of noise along the optical path. Optical fibers, while convenient for routing and alignment, are susceptible to phase fluctuations caused by temperature drifts, acoustic vibrations, and mechanical stress. Even small path length variations can lead to significant phase noise over meter-scale distances. Across the field, various techniques have been developed to address this issue. In some setups, piezo-mounted mirrors [19] or electro-optic modulators (EOMs) [20] are used in feedback loops to correct for phase fluctuations in free-space interferometers, while spatial light modulators (SLMs) [21] and deformable mirrors [22] are employed to correct spatial wavefront distortions in beam-shaping and quantum-gas experiments. In our system, we implement an active fiber-noise-cancellation (FNC) scheme by interfering the clock laser with the slave laser after it has been frequency shifted via an acousto-optic modulator (AOM). The resulting interference signal encodes phase noise accumulated along the fiber path, which is actively corrected by adjusting the AOM drive frequency. This approach offers a compact and robust solution for suppressing temporal phase fluctuations introduced during long-distance optical delivery.

Our laser system is intended to support not only atomic ion control, but also future experiments involving molecular ions. Molecules such as N_2^+ and I_2^+ possess a richer internal structure than atoms, including vibrational and rotational modes and different nuclear-spin isomers [23]. These features open the door to new forms of quantum-state control, encoding, and precision spectroscopy. One potential direction is the use of molecular ions in correlation spectroscopy with atomic clocks to probe variations in fundamental

constants [24], such as those that might arise from ultralight dark matter [25]. While such applications lie beyond the scope of this thesis, the laser system developed here is designed to meet the stability and resolution requirements that such measurements would demand.

In this thesis, we present the design, implementation, and performance of a 729 nm laser system based on injection locking and fiber-noise cancellation. Our work shows that significant spectral narrowing and phase coherence can be achieved through a simple, modular setup that leverages existing ultra-stable laser systems, without the need for in-lab cavities or frequency combs. By identifying and addressing phase noise introduced during delivery, and by ensuring RF stability within the FNC system, we create a platform suitable for coherent quantum control and precision spectroscopy. We characterize the laser system by measuring both in-loop and out-of-loop phase stability using interferometric techniques, and systematically scan the diode's injection parameters to optimize performance. We showcase the capabilities of this system through high-resolution spectroscopy on a single $^{40}Ca^{+}$ ion. This work represents a technical contribution to the broader effort to push the limits of resolution and coherence in atomic and molecular quantum systems.

2 Goals

The primary goal of this thesis is to develop a highly stable and narrow-linewidth laser at 729 nm for coherent quantum control of a single calcium ion (Ca^{+}). Achieving precise control over this transition is critical for future molecular-ion spectroscopy, where the Ca^{+} ion will serve as a quantum probe.

To accomplish this, the focus is on two key stabilization techniques:

1. **Laser Injection Locking** – Ensuring a high-quality injected laser with minimal frequency noise.
2. **Fiber-Noise Cancellation (FNC)** – Compensating for phase noise introduced during laser delivery through optical fibers.

The performance of our laser system will be characterized using interferometric methods and beat-stability analysis. Finally, we aim to achieve a spectroscopic signal of the clock transition in Ca^{+} using our laser system.

These advancements will enable high-fidelity gate operations on the 729 nm transition, ensuring precise control over the ion's quantum state and leading to improved spectral resolution and measurement accuracy. Ultimately, this work aims to establish a foundation for probing molecular ions with unprecedented accuracy, enabling new experiments in precision measurements and fundamental physics.

3 Methods - Injection Locking and Laser Stabilization

3.1 Injection Locking in Lasers

Injection locking is a laser stabilization technique in which a weak optical field from a master laser is injected into a slave laser. This process forces the slave's frequency, ω, and phase to lock to those of the master, provided the injection parameters lie within a defined locking range [26, 27]. Injection locking significantly reduces the slave laser's linewidth, suppresses phase noise, and improves spectral purity. In the following section, we derive the dynamical equations governing this locking behavior.

3.1.1 Maxwell–Bloch Equations

Applying the Slowly-Varying-Envelope Approximation (SVEA) to Maxwell's equations leads to a first-order wave equation for the field envelope coupled to the polarization, as derived in [28, Ch. 9]:

- **Electric-field envelope, $\mathcal{E}(t)$:**

$$\frac{d\mathcal{E}}{dt} + (L + i(\omega - \Omega))\mathcal{E} = -\frac{i\omega}{2\epsilon_0}P. \tag{1}$$

- **Polarization, $P(t)$:**

$$\frac{dP}{dt} + (i(\omega - \omega_0) + \gamma)P = i\frac{|\mu_{12}|^2}{\hbar}\Delta N\mathcal{E}. \tag{2}$$

- **Population inversion, $\Delta N(t)$:**

$$\frac{d\Delta N}{dt} = \frac{\Delta N_0 - \Delta N}{T_1} - \frac{2}{\hbar}\mathrm{Im}(P^*\mathcal{E}). \tag{3}$$

Here, ω is the field frequency, Ω is the cavity resonance frequency, ω_0 is the laser's two-level transition frequency, and $|\mu_{12}|$ is the dipole laser-field coupling. The parameters L, γ, and T_1 represent the cavity losses, polarization decay rate, and inversion relaxation time, respectively.

Neglecting Cavity Detuning The term $i(\omega - \Omega)$ in Eq. 1 accounts for a detuning between the field and the cavity resonance. In the regime of interest, where the laser oscillates close to the cavity resonance, we assume that this detuning is small compared to the cavity linewidth γ_{cavity}:

$$|\omega - \Omega| \ll \gamma_{cavity}.$$

Thus, the $i(\omega - \Omega)$ term can be neglected to leading order.

Adiabatic Approximation for the Polarization Since the polarization, P, typically relaxes much faster than the electric field $\mathcal{E}$, we apply the adiabatic approximation, neglecting dP/dt in Eq (2):

$$P \approx i\frac{|\mu_{12}|^2}{\hbar}\frac{\Delta N}{\gamma + i(\omega - \omega_0)}\mathcal{E}. \tag{4}$$

This shows that the polarization follows the electric field instantaneously. Putting Eq. (4) into Eq. (1) and neglecting the cavity-detuning term as mentioned above gives:

$$\frac{d\mathcal{E}}{dt} + L\mathcal{E} = \frac{\omega}{2\epsilon_0}\frac{|\mu_{12}|^2}{\hbar}\frac{\Delta N}{\gamma + i(\omega - \omega_0)}\mathcal{E}. \tag{5}$$

Dependence of the Inversion on Field Intensity The inversion dynamics are governed by Eq. (3). Assuming steady-state conditions ($d\Delta N/dt \approx 0$):

$$\Delta N = \Delta N_0 - T_1 \times \frac{2}{\hbar}\mathrm{Im}(P^*\mathcal{E}). \tag{6}$$

From Eq. (4), we find that $\mathrm{Im}(P^*\mathcal{E})$ is proportional to $\Delta N|\mathcal{E}|^2$. Therefore:

$$\Delta N = \Delta N_0 - \alpha|\mathcal{E}|^2, \tag{7}$$

where α is a constant depending on material and cavity parameters.

Relation Between Population Inversion and Gain Since the laser gain, G, is proportional to the population inversion, ΔN, we have:

$$G = G_0 - S|\mathcal{E}|^2, \tag{8}$$

where G_0 is the small-signal gain, and S is the saturation coefficient. Substituting this expression for G into the simplified field equation (5) leads to:

$$\frac{d\mathcal{E}}{dt} + (L - G_0 + S|\mathcal{E}|^2)\mathcal{E} = 0. \tag{9}$$

This is the Van der Pol equation for a free-running laser.

Addition of an Injected Field When an external weak field,

$$E_{\text{inj}}(t) = E_j e^{i\omega_j t}, \tag{10}$$

is injected into the laser cavity, the total electric field in the rotating frame is:

$$E_{\text{total}}(t) = \mathcal{E}(t) + E_j e^{i(\omega_j - \omega)t}. \tag{11}$$

Since the polarization, P, is driven linearly by the total electric field, it follows that:

$$\boxed{P \propto \Delta N \left(\mathcal{E}(t) + E_j e^{i(\omega_j - \omega)t}\right).} \tag{12}$$

Substituting back into the field equation, the injected field appears as a driving term.

Remark on the Role of the Injected Field In this derivation, the injected external field is incorporated by modifying the polarization, P, rather than by adding a term directly to the left-hand side of the field equation (1). This is consistent with the structure of Maxwell's equations (Sec. 3.1.1), where the material response (polarization) acts as a source term for the electric field. The left-hand side of the Maxwell–Bloch field equation describes the intrinsic dynamics of the cavity field $\mathcal{E}(t)$, including propagation losses and possible detuning.

External fields interact with the gain medium by modifying its polarization. This altered polarization then acts back on the intracavity field through the right-hand side of the field equation. Therefore, the injected field enters the laser dynamics by perturbing the polarization, P, not by directly altering the free evolution of the cavity field.

The final forced Van der Pol equation reads [28, 29]:

$$\boxed{\frac{d\mathcal{E}}{dt} + (L - G_0 + S|\mathcal{E}|^2)\mathcal{E} = K_j E_j e^{i(\omega_j - \omega)t}} \tag{13}$$

where K_j is a coupling coefficient depending on the medium and cavity properties.

3.1.2 Adler's Equation

Starting from the forced Van der Pol equation (13), we express the complex field as:

$$\mathcal{E}(t) = A(t)e^{i\phi(t)}, \tag{14}$$

where $A(t)$ and $\phi(t)$ are real functions representing the amplitude and phase of the field. Differentiating the above equation yields:

$$\frac{d\mathcal{E}}{dt} = \left(\frac{dA}{dt} + iA\frac{d\phi}{dt}\right)e^{i\phi}. \tag{15}$$

Since the injected field oscillates as $e^{i(\omega_j - \omega)t}$ relative to the cavity frame, we define the slowly varying phase difference:

$$\theta(t) = \phi(t) - (\omega_j - \omega)t, \tag{16}$$

thus:

$$\phi(t) = \theta(t) + (\omega_j - \omega)t \quad \text{and} \quad \frac{d\phi}{dt} = \frac{d\theta}{dt} + (\omega_j - \omega). \tag{17}$$

Substituting this definition into the field equation and matching real and imaginary parts yields:

- **Amplitude equation:**

$$\frac{dA}{dt} + (L - G_0 + SA^2)A = K_j E_j \cos(\theta). \tag{18}$$

- **Phase equation:**

$$A\left(\frac{d\theta}{dt} + (\omega_j - \omega)\right) = -K_j E_j \sin(\theta). \tag{19}$$

Assuming the amplitude A relaxes rapidly to steady state, we set $dA/dt \approx 0$, yielding:

$$(L - G_0 + SA^2)A = K_j E_j \cos(\theta), \tag{20}$$

which implies that A depends slowly on θ.

Substituting into the phase equation gives:

$$\frac{d\theta}{dt} = -(\omega_j - \omega) - \frac{K_j E_j}{A} \sin(\theta). \tag{21}$$

Defining:

$$\Delta\omega = \omega - \omega_j \quad \text{and} \quad \kappa = \frac{K_j E_j}{A}, \tag{22}$$

the phase dynamics reduce to the Adler equation:

$$\boxed{\frac{d\theta}{dt} = \Delta\omega - \kappa \sin(\theta),} \tag{23}$$

which governs the phase evolution of the injection-locked laser.

Locking Range and Frequency Pulling Adler's equation provides the condition for stable phase locking:

$$\sin\theta = \frac{\Delta\omega}{\kappa}. \tag{24}$$

Since $|\sin(\theta)| \leq 1$, the detuning must be smaller than the coupling strength to achieve steady-state conditions, $d\theta/dt = 0$. The maximum detuning for stable locking defines the locking range:

$$\Delta\omega_{\text{lock}} \approx 2K_j\sqrt{R}, \tag{25}$$

where $R = P_{\text{master}}/P_{\text{slave}}$ is the injection ratio [27, 30]. Within this range, the slave laser inherits the master's spectral purity, reducing its linewidth.

Linewidth Narrowing and Spano's Noise Model The frequency noise spectrum of an injection-locked laser follows the expression derived by Spano et al. [18]:

$$S_{\Delta\nu}(\Omega) = S_{\Delta\nu,M}(\Omega) + \left(\frac{\Omega^2}{\kappa^2}\right) S_{\Delta\nu,S}(\Omega), \tag{26}$$

where:

- $S_{\Delta\nu,M}(\Omega)$ is the frequency-noise spectrum of the master laser,
- $S_{\Delta\nu,S}(\Omega)$ is the frequency-noise spectrum of the free-running slave laser,
- κ is the locking strength, determined by the injection power and cavity parameters,
- Ω is the Fourier frequency offset from the carrier.

At low Fourier frequencies ($\Omega \ll \kappa$), the spectral properties of the master laser dominate, ensuring that its stability is effectively transferred to the slave. This occurs because the injected field forces the slave laser's phase to follow that of the master, suppressing its intrinsic phase noise. As the Fourier frequency increases ($\Omega \gg \kappa$), the influence of the master diminishes, and the slave laser's inherent noise begins to dominate.

The coupling efficiency, κ, plays a crucial role in determining the effectiveness of injection locking and depends strongly on transverse-mode matching and slave diode cavity quality. A well-matched transverse-mode profile between the master and slave lasers ensures efficient spatial overlap, allowing optimal power transfer and minimizing losses due to beam mismatches. Additionally, a high-quality slave laser cavity with low internal losses and a well-defined longitudinal-mode structure enhances its ability to maintain coherence with the injected field, reducing phase noise and improving locking stability.

Stronger injection not only enhances noise suppression but also extends the locking range, as shown in equation 25, allowing the slave laser to remain frequency-locked over a broader detuning range.

3.2 I-V Characteristics of a Laser Diode and its Temperature Dependence

Once the slave diode current exceeds the threshold current, I_{th}, stimulated emission dominates, and the I-V characteristics of the diode deviates from the simple diode equation (see Appendix 8.1 for more details). The total voltage can be expressed as:

$$V = IR_s + V_{\text{th}}, \tag{27}$$

where:

- R_s is the series resistance of the laser diode.

In this regime (see Appendix 8.1):

- The diode voltage increases slowly with current.
- The differential resistance (dV/dI) is significantly lower than at low current levels.
- The optical output power increases linearly with excess current:

  $$P_{\text{opt}} = \eta_d(I - I_{\text{th}}),$$

  where η_d is the differential quantum efficiency.
- I_{th} is the threshold current, the minimum current required for lasing.

3.2.1 Temperature Dependence via Power Dissipation

The temperature of the laser diode is influenced by Joule heating, which depends on the electrical power dissipated:

$$P_{\text{heat}} = IV - P_{\text{opt}}. \tag{28}$$

For efficient lasers, where a significant portion of the input electrical power is converted into optical output, the heat dissipation is reduced. However, for typical diodes:

$$T(I) = T_0 + R_{\text{th}}P_{\text{heat}}, \tag{29}$$

where R_{th} is the thermal resistance of the diode. Since V is nearly constant above threshold (see Appendix 8.1.2), the temperature dependence primarily follows:

$$T(I) \approx T_0' + \Theta \cdot I \quad \text{where} \quad \Theta = R_{\text{th}}V_{\text{th-opt}}. \tag{30}$$

Thus, temperature increases with electrical power dissipation, impacting the bandgap, emission wavelength, and injection locking conditions. Controlling I and P_{opt} is crucial for laser stability and thermal management.

The emission wavelength of the laser is determined by the semiconductor bandgap energy, $E_g(T)$, which varies with temperature due to phonon interactions. At high temperatures ($T \gg T_D$, where T_D is the Debye temperature), this dependence follows [31–34]:

$$E_g(T) \approx E_g(0) - \gamma k_B T \tag{31}$$

Where, γ, is an empirical parameter defined in [31]. Since the emission wavelength, λ, is related to the bandgap energy as:

$$\lambda(T) = \frac{hc}{E_g(T)}, \tag{32}$$

substituting $E_g(T)$ gives a linear wavelength shift with temperature:

$$\lambda(T) \approx \lambda_0 + \frac{\gamma k_B \lambda_0^2}{hc} T. \tag{33}$$

This equation shows that as temperature increases, the emission wavelength redshifts, which directly affects the injection locking condition. Apart from bandgap narrowing, the cavity resonance modes shift with temperature due to the thermal expansion of the laser cavity:

$$L(T) = L_0(1 + \alpha_L(T - T_0)), \tag{34}$$

where L_0 is the cavity length at a specified temperature, T_0, and α_L is the linear coefficient of thermal expansion. The longitudinal cavity modes satisfy the condition:

$$m\frac{\lambda}{2} = L(T), \tag{35}$$

where m is the longitudinal-mode index. Differentiating with respect to T gives:

$$\frac{d\lambda}{dT} = \frac{2}{m}\frac{dL}{dT} = \frac{2}{m} L_0 \alpha_L, \tag{36}$$

which implies that for linear expansion of the cavity, also the wavelength will depend linearly on the temperature. For InGaAsP materials lattice-matched to InP (as used in the HL7301MG diode that we are using), the linear thermal expansion coefficient is on the order of $\alpha_L \approx 5.1 \times 10^{-6}$ K^{-1} [35], supporting the use of a linear model across the diode's operating range.

The above discussion shows that the laser wavelength shifts proportionally with temperature through both bandgap narrowing and thermal expansion. These relations explain the dependence of injection locking on current and temperature.

3.3 Fiber-Noise-Cancellation (FNC) Method

3.3.1 Optical-Path Length and Fluctuations

Fluctuations in the optical fiber arise due to several environmental effects:

- **Temperature variations**: Changes in the refractive index and fiber length introduce slow drifts [36].
- **Mechanical vibrations**: Structural motion and acoustic disturbances cause dynamic fluctuations [37].

These variations lead to changes in the optical path length, defined as:

$$\mathrm{OPL}(t) \;=\; \int_0^L n\big(z,t\big)\,\mathrm{d}z, \tag{37}$$

where $n(z)$ denotes the refractive index along the fiber axis. Since the light is confined to the fiber, the integral runs simply from $z = 0$ to $z = L$. The associated phase is therefore given by:

$$\phi_{\mathrm{fiber}}(t) = \frac{2\pi}{\lambda}\mathrm{OPL}(t), \tag{38}$$

which degrade coherence and require active compensation.

3.3.2 AOM-Based Noise Cancellation

The fiber-induced fluctuations manifest as phase variations on the interference signal. These fluctuations are extracted as an electrical error signal using a phase detector. This error signal reflects the deviation between the expected and actual phase evolution of the light returning from the fiber.

To correct this error, a proportional-integral (PI) controller is applied:

$$V(t) = G_P \cdot \text{error}(t) + G_I \cdot \int_0^t \text{error}(t')\, dt', \tag{39}$$

where G_P and G_I are the proportional and integral gains, respectively.

This control voltage drives a voltage-controlled oscillator (VCO), which sets the frequency of the AOM. With a linear tuning response, the AOM frequency at time t is given by:

$$f_{\text{AOM}}(t) = \kappa \left(V_0 + V(t)\right), \tag{40}$$

where V_0 is a static bias voltage, $V(t)$ is the PI controller output, and κ is the VCO tuning coefficient in units of Hz/V.

The system is biased such that $\kappa V_0 = 40\,\text{MHz}$, which defines the nominal operating point of the AOM. The correction term, $\kappa V(t)$, dynamically compensates for the fiber-induced phase fluctuations. This feedback loop ensures that the AOM frequency tracks the accumulated noise and stabilizes the optical phase at the output [38].

3.3.3 Performance and Stability Considerations

Fiber noise cancellation systems demonstrated suppression of fluctuations over a broad frequency range, typically up to 20 kHz, as confirmed by experimental data [39]. Key factors influencing system performance include:

- **Loop response time**: The PLL must be fast enough to track and correct dominant noise sources [37].
- **Residual noise sources**: Imperfections in detection and feedback electronics introduce minor fluctuations [38].
- **Long-term stability**: Temperature-induced drift may require additional low-bandwidth correction mechanisms [36, 40].

By dynamically adjusting the AOM frequency, this approach can achieve high-fidelity noise suppression, significantly improving the stability of optical transmission systems [39].

3.4 Laser Linewidth Estimation Using the Beta Separation Method

3.4.1 Phase Noise to Frequency Fluctuation Conversion

To evaluate the contribution of laser frequency noise to its linewidth or spectral properties, it is common to convert the **phase noise** $S_\phi(f)$ (typically given in dBc/Hz) into the **frequency noise power spectral density** $S_\nu(f)$ in units of Hz^2/Hz. The relationship is [40]:

$$S_\nu(f) = \left(\frac{2}{f^2}\right) 10^{S_\phi(f)/10}. \tag{41}$$

In this expression, f denotes the offset frequency in Hz, $S_\phi(f)$ is the single-sideband phase noise expressed in dBc/Hz, and $S_\nu(f)$ is the resulting frequency fluctuation PSD in Hz^2/Hz.

3.4.2 Linewidth Estimation via the β-Separation Method

A precise determination of the laser linewidth is essential for optimizing system performance in frequency stabilization and coherent optical processes. In this thesis, we employ the β-separation method to extract the linewidth from the **power spectral density (PSD) of frequency fluctuations**. This method provides

a systematic approach to distinguish between the spectral components that contribute to the linewidth and those that influence only the wings of the laser line shape. The **β-separation line**, given by [41]:

$$S_{\nu,\beta}(f) = 8(\ln 2)\frac{f}{\pi^2}, \tag{42}$$

separates the **high-modulation-index region**, which significantly contributes to the linewidth, from the **low-modulation-index region**, which affects only the spectral wings. The **β-separation frequency**, f_β, is the offset frequency where the measured $S_\nu(f)$ intersects with $S_{\nu,\beta}(f)$.

To compute the **laser linewidth $\Delta\nu$**, we integrate the frequency noise PSD **from the lowest measured, $f_{\min}$, frequency up to the β-separation frequency**:

$$\Delta\nu = \sqrt{8\ln 2 \int_{f_{\min}}^{f_\beta} S_\nu(f)df}, \tag{43}$$

This integral captures the contribution of frequency noise within the coherence bandwidth of the laser, ensuring that only the **relevant spectral components** contributes to linewidth estimation while excluding noise that merely affects the spectral wings.

4 Results - Injection Locking and Laser Stabilization

4.1 The Laser System

The system is designed to transfer a highly coherent Hz-linewidth laser at 729 nm from a remote lab to our lab while suppressing fiber-induced noise. In our lab, the weak signal from the remote lab is amplified using an injection setup. The amplified signal is then directed to the ion-trapping experiment. The setup consists of an acousto-optic modulator for fiber-noise cancellation (AOM-FNC) followed by a 120 m optical fiber link connecting the two labs. Another AOM controls the exact frequency of the amplified light that reaches the ion. The laser light undergoes the following path (see Fig. 1):

1. A narrow-linewidth coherent laser light at $f_0 = 411.0421443$ THz from a master laser in a remote lab (Roee Ozeri's clock lab) enters our FNC system with H polarization and directed into a shear-type AOM-FNC modulated at 40 MHz (green arrow).
2. The 0^{th}-order non-diffracted beam with H polarization is reflected back to the AOM-FNC (green arrows) where it diffracts to the $+1^{\text{st}}$ order with V polarization (blue arrow).
3. The -1^{st}-order diffracted beam with V polarization propagates from the remote lab to our lab through 120 m of fiber (red arrows).
4. The light is then directed through a side port of an isolator (path (1)) to the slave laser where it is amplified by injection (red arrows).
5. Small fraction of the light from the injected slave diode returns through the isolator side port (path (1)) back to the remote lab where it passes the AOM-FNC without diffracting (red arrows).
6. This slave light interferes with the reflected master light (red/blue arrow) on a photodetector, creating the phase error signal.
7. The AOM-FNC is phase-locked using a PLL, dynamically adjusting its frequency to compensate for fiber-induced fluctuations.
8. Most of the light from the injected slave diode goes through the isolator (path (2)) to the experimental AOM setup (∼220 MHz, -1^{st} order) in a double pass configuration where it is shifted to match one of the $^{40}Ca^{+}$ lines.

This scheme ensures that any fluctuations accumulated in the fiber are mapped onto the interference signal and actively corrected in real time.

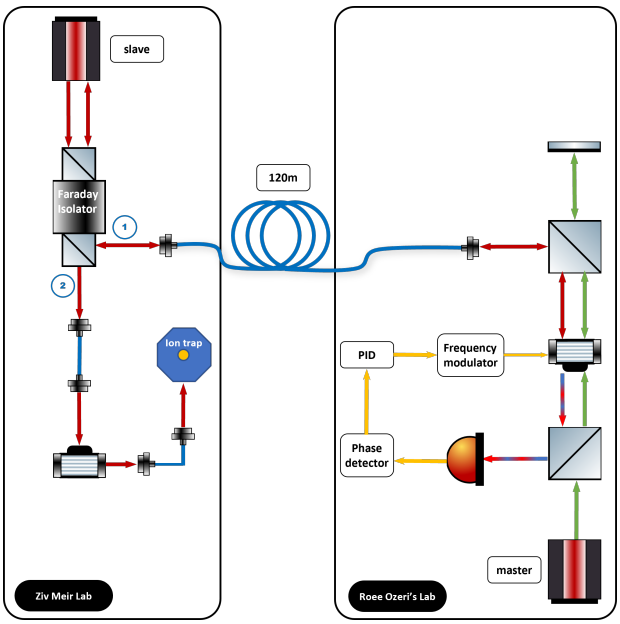

Figure 1: Schematic of the laser system including the fiber noise cancellation setup, injection diode, and experimental AOM setup.

The Physical Setup Fig. 2 shows the optical setup we constructed. Paths (a) and (d) correspond to the fiber noise cancellation and injection locking lines, as depicted in Fig. 1. Path (b) delivers light to the double-pass AOM setup and ultimately to the ion trap. Path (c) leads to the wavelength meter.

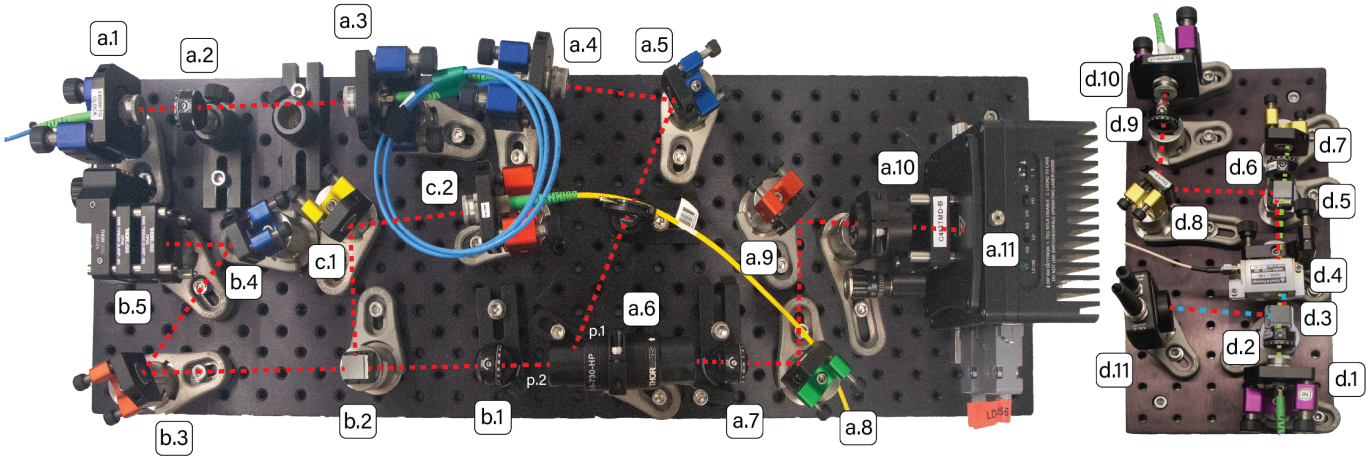

Figure 2: Labeled photograph of the optical setup used for laser injection and fiber noise cancellation.
(a.1–a.3): A short diagnostic line used to measure coupling from the master laser in the remote lab to our lab and to control polarization. In addition, it is used to measure the spatial coupling of the master and slave lasers. Typical powers are 1 mW for the master and 0.5 mW for the slave.
(a.4–a.6): Alignment optics for matching the slave beam into the spatial mode of the master by maximizing the input coupling of the slave laser to the fiber coupler (a.4). The master (slave) beam enters (exists) the isolator (a.6) through port p.1.
(a.7–a.11): Spatial mode shaping optics for the master/slave lasers. The anamorphic prism pair (a.10) corrects for the natural ellipticity of the slave beam.
(b.1–b.2): Optical path controlling the ratio of power between the wavemeter and the main experiment.
(b.3–b.5): Fiber coupling line for the main laser line, delivering up to 50 mW to the experiment.
(c.1–c.2): Coupling to the wavemeter, typically with 0.5 mW of power.
(d.1): Fiber input from the master (clock) laser.
(d.3): A beamsplitter that transmits the clock laser in the forward direction and reflects the interference signal in the backwards direction (red and blue lines) toward the photodiode (d.11).
(d.4): A 40 MHz shear-AOM configured for 50% diffraction efficiency, producing both -1^{st} (red, V polarization) and 0^{th} (green, H polarization) orders.
(d.5): Order-splitting PBS separating the AOM outputs, and combining the AOM inputs.
(d.6–d.7): Mirror and wave plate controlling the amount of master light reflected back to the AOM to create the interference.
(d.8–d.10): Fiber coupling between the master and slave systems, connected via a 120 m optical fiber between d.10 and a.1.
(d.11): FNC photodiode. Detects the interference between the return slave signal (shifted by -40 MHz) and the return master signal (shifted by +40 MHz).

4.2 Injection-Locking characterization

To properly inject the slave laser we require that (see Sec. 3.1.2): 1) Good spatial mode overlap between the master signal and the slave laser. 2) Spectral overlap between the master signal and one of the slave modes. 3) Enough power to saturate the injection.

To evaluate the quality of the injection lock, we developed a diagnostic method based on monitoring the interferometric signal from the wavemeter (HighFinesse WS8-10). A well-injected laser produces a clean and stable interference pattern, as shown in Fig. 3c. By varying the temperature and current of the slave diode—either manually or via automated control—we searched for operating points that yield sharp and periodic interference fringes. For these injection-locking conditions, we found out that the wavelength reading deviation from nominal was less than $|\Delta\lambda| \approx 10^{-5}$ nm. The deviation is attributed to wavemeter calibration drifts.

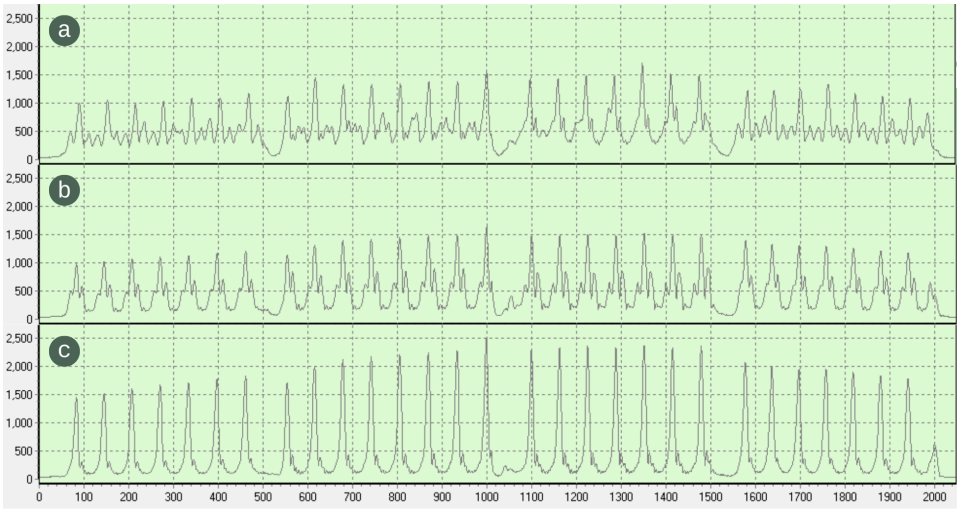

Figure 3: Interferometric signal from the wavemeter (HighFinesse WS8-10) used to assess injection quality. (a) No injection: only the master laser is present, resulting in a weak and irregular pattern. (b) Partial injection: the slave is injected but with suboptimal parameters, producing unstable fringes. (c) Optimal injection: strong, periodic fringes indicate a well-injected slave laser.

4.2.1 Current and Temperature dependence

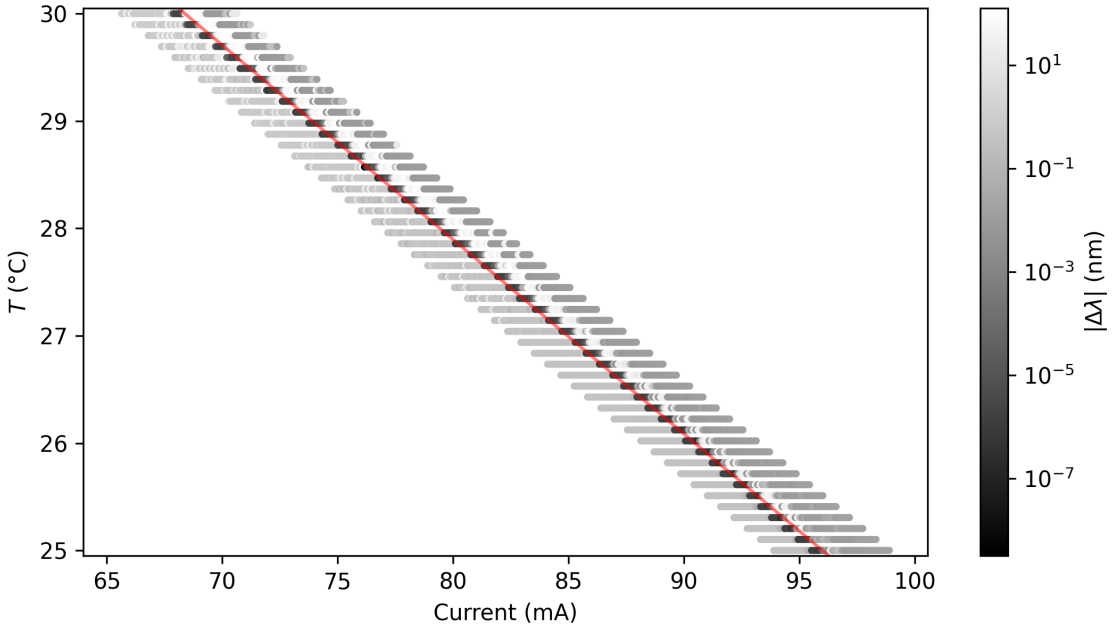

Figure 4: Injection-locking map for the slave diode. The vertical axis indicates the diode's temperature, T, while the horizontal axis its drive current, I. The gray scale represents deviations of the slave laser from the master laser wavelength (logarithmic scale). An injection-locked laser is indicated by the dark band which corresponds to $|\Delta\lambda| < 10^{-5}$ nm. The residual wavelength deviation is attributed to wavemeter calibration drifts. The fitted line (red) follows $T = T_0' + \Theta\, I$, where $T_0' = 42.382°\text{C}$ and $\Theta = -0.181°\text{C/mA}$. It describes the diode's linear temperature-current setpoint for robust locking.

In Fig. 4, we plot the locking region dependence on both the slave diode temperature, T, and current, I. A key outcome is that the locking region follows a linear relationship:

$$T = T_0' + \Theta\, I, \tag{44}$$

where T_0' is the baseline temperature at zero current, and Θ describes how T must shift with I to maintain lock. This relationship is identical to the relation of the diode's temperature with its driving current (see

Eq. 30). This implies that we are able to keep the total temperature of the diode (gain medium and cavity) constant.

Fitting the results presented in Fig. 4 (red line) we get,

$$T_0' = 42.382\,^\circ\mathrm{C}, \quad \Theta \ = -0.181\,^\circ\mathrm{C/mA}.$$

Operating along this linear trend allows the slave to remain on exact resonance with the master-laser wavelength. The small deviations in the wavemeter readings corresponds to instrumental drifts of the wavelength measurement by the wavemeter. From an experimental perspective, these data confirm that carefully matching T and I can preserve injection. We can choose the desired diode operating point with respect to output power at a reasonable operating temperature.

4.2.2 Injection-Locking Range and Saturation

In Fig. 5, we measured the diode's locking range as function of the injected optical power from the master laser. The slave-laser power and master-laser power were monitored at points (1) and (2) in Figure 1, respectively. The locking range reveals a near-linear rise in the locked current window up to injection ratio of $R = P_{\mathrm{master}}/P_{\mathrm{slave}} \approx 0.003$, followed by saturation. This observation does not fully align with the relation in 25, as it is based on a rather simplistic model.

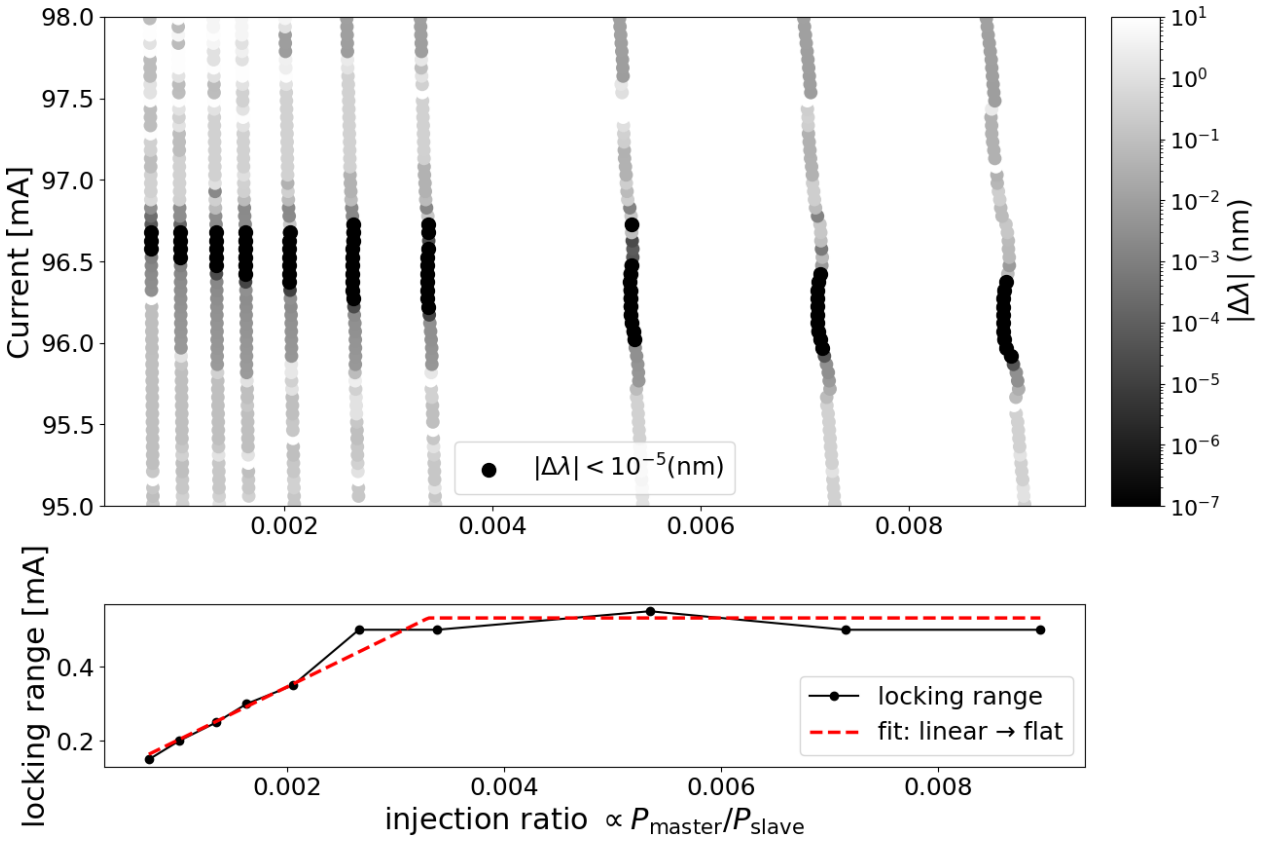

Figure 5: Injection lock range as function of injected power ratio. (Top) Raw data of the measured wavelength difference $|\Delta\lambda|$ as a function of slave-laser current (y-axis) and injected power ratio (x-axis). The logarithmic gray scale highlighting points within $|\Delta\lambda| < 10^{-5}$ nm where the laser is considered injection locked. (Bottom) The extracted current-locking range plotted against the injection power ratio $R \propto P_{\mathrm{master}}/P_{\mathrm{slave}}$. Mode hops are observed near the edges of the locking region, underscoring the importance of operating within the main plateau for robust, stable locking. Dashed red line is fitted to a linear and flat regions.

The saturation regime has two practical implications. First, once the injection coupling is strong enough, adding more power does not further expand the locking range. Second, operating near or above this saturation point makes the system resilient to small fluctuations in injected power, such as those caused by

fiber-related polarization and amplitude noise. In this high-coupling regime, minor power drifts due to environmental or fiber instabilities do not appreciably degrade the slave-laser lock, resulting in a robust and stable output despite imperfect power regulation.

4.3 Fiber-Noise Cancellation measurements

Fig. 6 illustrates the measurement setup for characterizing the fiber-noise-cancellation performance. A single laser source is split by a beam splitter into two paths: a *fiber arm* and a *reference arm*. The fiber arm passes through the FNC setup that includes a 5 m spool with its output on the same optical table of the source. The reference arm provides a stable local oscillator. The FNC photodiode records the 80 MHz *in-loop* signal. However, this setup also features an *out-of-loop* signal at 40 MHz between the reference arm and the signal that output the fiber spool. These two beams are recombined to produce a beat note whose frequency fluctuations encode the fiber's phase noise.

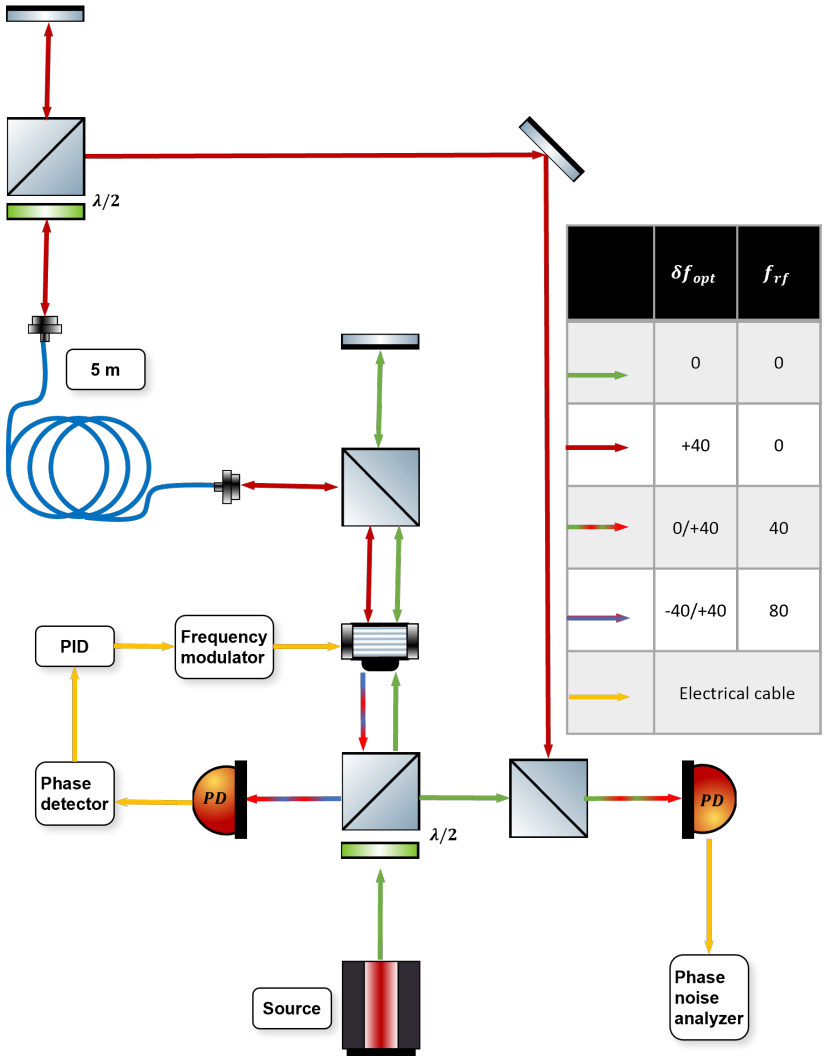

Figure 6: Schematic of the out-of-loop phase-noise measurement. The PID loop (yellow) corrects the frequency modulator to stabilize the beat note against fiber fluctuations measured on the left photodiode (PD). The right PD monitors the (*out-of-loop*) noise between the light that passes through the fiber and the original signal. Arrows color indicate the optical frequency deviation, δf_{opt}, and the beat frequency, f_{rf} (see legend).

4.3.1 Out-of-Loop Results

A *phase noise analyzer* (Microchip 53100A) measures the beat note's phase-noise spectrum; specifically, it outputs the power spectral density (PSD) of phase fluctuations by using TimeLab software. From this PSD (dBc/Hz), we compute the equivalent frequency fluctuations $S_\nu(f)$ in units of $\mathrm{Hz}^2/\mathrm{Hz}$ using 41. The PID servo actively locks the beat note by driving the frequency modulator, thus canceling much of the

fiber-induced phase noise in real time. Crucially, we place an *out-of-loop* photodiode and phase detector so that this second detector's signal is *not* used by the PID; this ensures our measurement genuinely reflects the final noise, uncorrupted by any feedback-loop artifacts.

To quantify the servo's effectiveness, we record two datasets:

1. **Locked (PID On):** The servo engages, suppressing phase noise from the fiber.
2. **Unlocked (PID Off):** The fiber noise remains uncompensated, providing a baseline.

In Fig. 7, we show the resulting PSD of the frequency fluctuations in both locked (blue) and unlocked (red) conditions on a log–log scale. We also plot the so-called β*-separation line* (Sec. 3.4.2), which discriminates between: high modulation index regime ($S_\nu(f) > S_{\nu,\beta}(f)$) where the PSD contributes to the linewidth, and a low modulation index regime ($S_\nu(f) < S_{\nu,\beta}(f)$) where the PSD contributes only to the wings of the line shape. The area under each curve (up to the β-separation frequency, f_β) is integrated to estimate the effective laser linewidth (Eq. 43). We see that the estimated linewidth for the locked laser (∼30 Hz) is 3 order of magnitude narrower than the estimated linewidth of the unlocked laser (∼50 kHz).

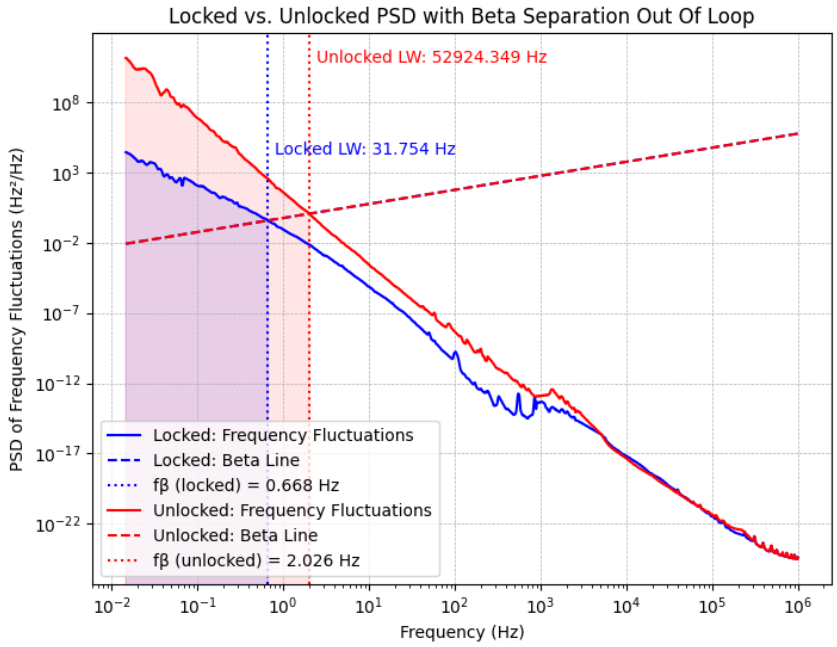

Figure 7: Locked vs. unlocked frequency-fluctuation PSD, measured via the out-of-loop photodiode and phase-noise detector. The shaded regions illustrate the integration bounds for estimating the linewidth.

At low offset frequencies (around 0.1 Hz), the locked trace lies substantially below the unlocked trace, indicating up to 40dB of noise suppression. This out-of-loop method demonstrates that the PID loop effectively reduces fiber phase noise across a broad frequency range (up to ∼1 kHz), and that our measurement truly reflects the residual noise outside of the loop's direct feedback path. Verifying the laser performance is crucial before integrating the system into the main experiment, where stable, low-noise laser delivery is vital. It is important to emphasize that this measurement does not constitute a full characterization of the FNC system capabilities. Firstly, the source laser used here is an injection-locked diode laser with an unknown intrinsic linewidth, in contrast to the clock laser employed in the main experiment. This may introduce uncorrelated phase noise between the unshifted and the 40 MHz frequency-shifted beams. Secondly, the 5-meter fiber spool used in this setup was placed in a temperature-stabilized and acoustically isolated room. This substantially suppresses both mechanical stress-induced phase fluctuations and acoustic noise. In contrast, in our main setup (see Fig. 1), the fiber experiences a less controlled environment and is therefore more susceptible to such perturbations.

4.3.2 In-Loop Results

The *in-loop* noise measurements were performed on the finalized setup (Fig. 1) with the 120 m fiber connecting between the labs. The light path to the FNC photodiode is described in detail in Sec. 4.1. The

resulting interference signal exhibits a visibility exceeding 90%.

In Fig. 8, we present the RF spectra of the optical beat signal obtained from the spectrum analyzer ('Keysight-N9010A'), in both the unlocked and locked cases. In the unlocked case (cyan), the *in-loop* linewidth is approximately 10 kHz, while in the locked case (orange), the signal is significantly narrower. The right-hand panel shows a high-resolution measurement of the locked peak, confirming that its *in-loop* linewidth is below the 1 Hz resolution bandwidth of the spectrum analyzer.

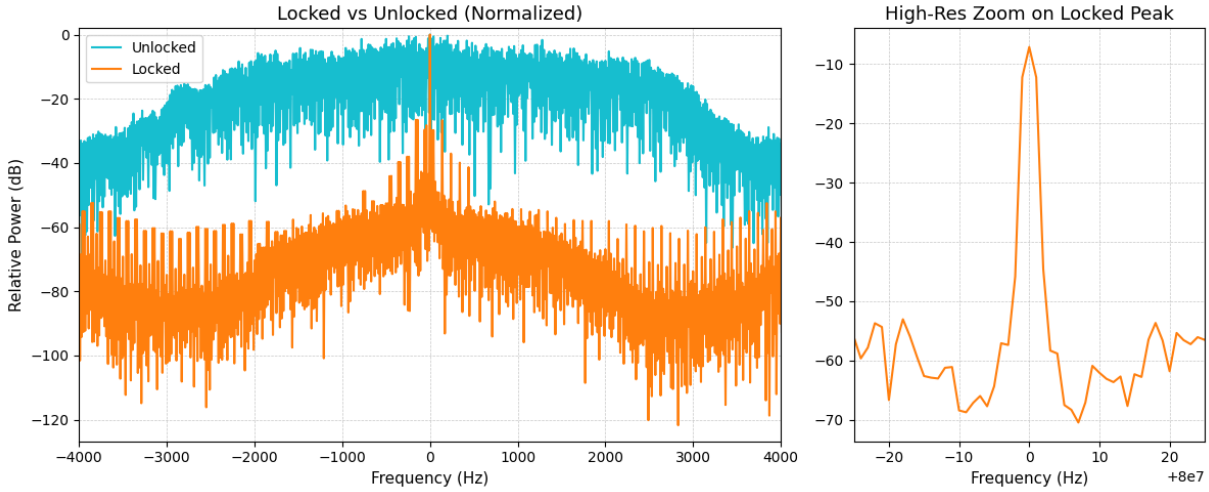

Figure 8: RF spectrum of the optical beat signal. **Left:** Unlocked (cyan) and locked (orange) signals, normalized and aligned to their respective carrier frequencies. **Right:** High-resolution trace of the locked signal showing a linewidth below the analyzer's 1 Hz resolution.

Next, we recorded the beat signal using a frequency counter with a 1-second gate time, and from this data we extracted the Allan deviation (ADEV) and modified Allan deviation (MDEV), shown in Fig. 9. The Allan and modified Allan deviation data reveal key features of the noise behavior in the locked system. In the short to intermediate averaging regime ($\tau \in [1, 270]$ s), the modified Allan deviation follows a slope of approximately -0.588, which is characteristic of white frequency modulation (WFM). At longer averaging times ($\tau \in [400, 2500]$ s), the slope steepens to -1.475, approaching the -1.5 value expected for white phase modulation (WPM). The lowest measured MDEV drops below 10^{-19} at $\tau = 1000$ s, suggesting excellent long-term stability between the injected and source lasers.

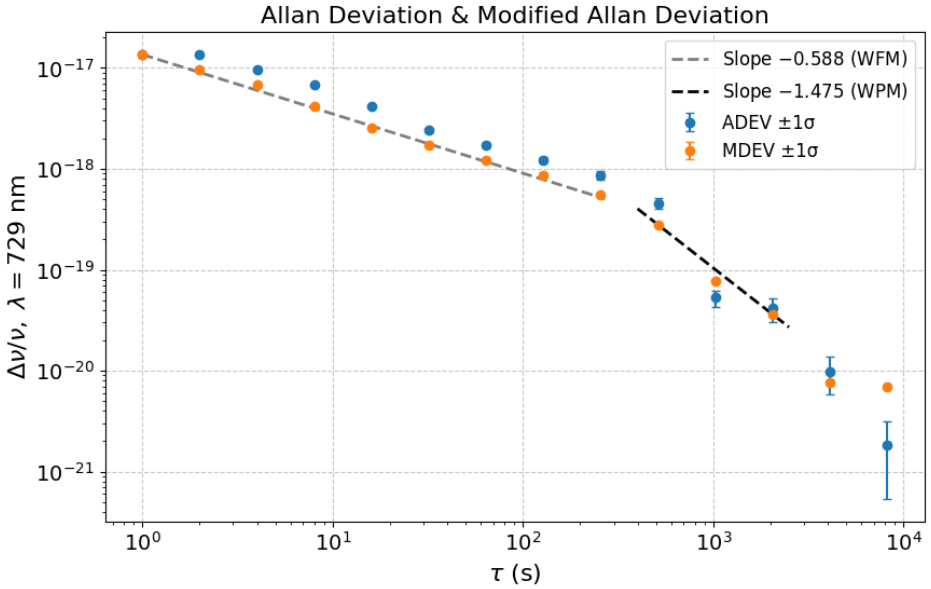

Figure 9: Allan deviation (ADEV) and modified Allan deviation (MDEV) of the locked beat signal. The dashed lines show fitted power-law slopes: -0.588 for short to intermediate timescales ($\tau \in [1, 270]$ s), and -1.475 at longer timescales ($\tau \in [400, 2500]$ s).

5 Methods - Coherent Manipulation of the $^{40}Ca^{+}$ Quadrupole Transition

5.1 The Electric Quadrupole Transition in $^{40}Ca^{+}$

The $^2D_{5/2}$ level in singly-ionized calcium ($^{40}Ca^{+}$) is a metastable state with a lifetime of approximately 1 second [42]. This long-lived character stems from the fact that the $4s\,^2S_{1/2} \leftrightarrow 3d\,^2D_{5/2}$ transition is electric-dipole forbidden and instead proceeds via the much weaker electric-quadrupole interaction. Compared to dipole-allowed transitions with nanosecond-scale lifetimes and MHz-scale linewidths, this quadrupole transition is about nine orders of magnitude longer in its lifetime and narrower in its natural linewidth.

The natural linewidth, $\Delta\nu_{\text{nat}}$ (in Hz), is inversely related to the excited state lifetime, τ, by:

$$\Delta\nu_{\text{nat}} = \frac{1}{2\pi\tau}. \tag{45}$$

With $\tau = 1.168$ s [43], this yields a natural linewidth of approximately $\Delta\nu_{\text{nat}} \approx 0.14$ Hz. This makes the 729 nm quadrupole transition between the $^2S_{1/2}$ ($|S\rangle$) and the $^2D_{5/2}$ ($|D\rangle$) states an ideal candidate for applications requiring extremely narrow and coherent optical transitions.

In the context of ion trapping and laser cooling, the long-lived $|D\rangle$ state enables high-fidelity state preparation and readout, long coherence times, and precise manipulation of internal states using narrowband laser light. These properties are essential both for quantum information processing [44]—where the $|S\rangle$ and $|D\rangle$ levels form a stable optical qubit—and for precision spectroscopy, such as in the development of optical clocks [45].

To fully utilize this potential, the addressing laser must exhibit a linewidth significantly narrower than the power-broadened linewidth of the transition, rather than the natural linewidth itself. In typical quantum logic and coherent control experiments, the effective linewidth is set by the Rabi frequency (which is proportional to the inverse of the interaction time) which is much larger than the natural linewidth. For example, for Rabi oscillations with a μs to ms timescale, the corresponding Fourier-limited linewidth is on the order of MHz to kHz respectively. A laser linewidth much narrower than this power-broadened width is necessary to avoid introducing decoherence during driven Rabi or Ramsey sequences. In practice, narrow-linewidth lasers with stabilities on the order of a few Hz or better have enabled coherence times exceeding several hundred milliseconds in similar systems [46].

Beyond internal-state control, the 729 nm laser also enables quantum logic operations through resolved sideband transitions [47]. In the Lamb-Dicke regime, where the ion's motion is confined to less than the optical wavelength, the laser can couple internal electronic states with quantized vibrational modes of the ion in the trap. This sideband excitation mechanism is the basis for entangling gates [48], ground-state cooling [49], and precise motional control—core ingredients for trapped-ion quantum computation. The spectral resolution and stability of the 729 nm laser are therefore critical not just for maintaining coherence, but also for addressing motional sidebands with high fidelity.

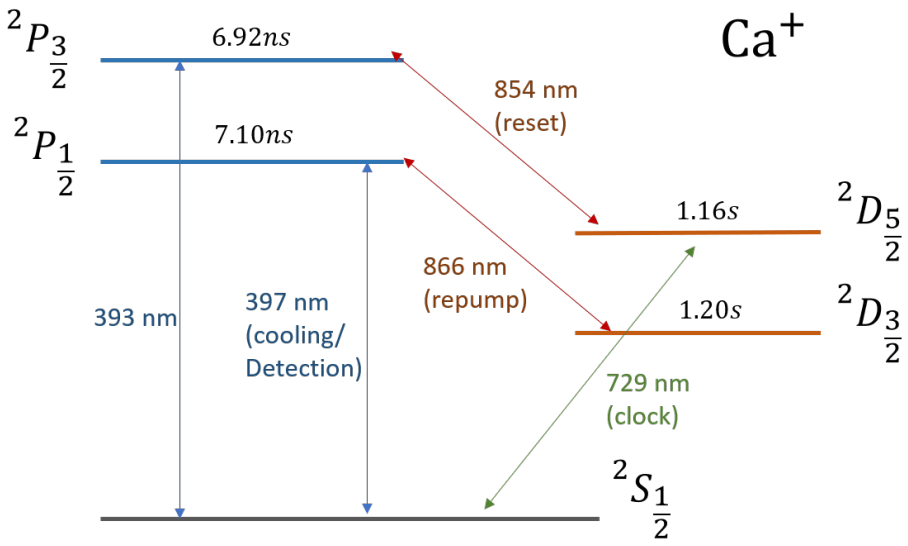

Figure 10: Simplified level diagram of $^{40}Ca^{+}$ showing all relevant transitions and annotated with lifetimes [50]. The metastable $^2D_{5/2}$ state (used for the 729 nm clock/qubit transition) is orders of magnitude longer-lived than the dipole-allowed $^2P_{1/2}$ state used for cooling and detection.

Other levels in the $^{40}Ca^{+}$ system are also involved in the cooling and detection scheme. The $^2P_{1/2}$ and $^2P_{3/2}$ levels have lifetimes of approximately 7.1 ns and 6.9 ns, respectively, and the $^2D_{3/2}$ level has a lifetime of about 1.2 s—comparable to that of $^2D_{5/2}$ [50]. These states support fast optical pumping and rapid cooling on strong dipole-allowed transitions, such as the 397 nm and 866 nm lines, enabling efficient state initialization and detection. The dramatic difference in timescales between the dipole and quadrupole transitions is what allows the system to combine both fast control and long-time coherence, as summarized in Figure 10.

The narrow linewidth of the 729 nm transition allows the resolution of individual Zeeman sublevels within the $^2S_{1/2}$ and $^2D_{5/2}$ manifolds under a modest external magnetic field. In a static field of a few Gauss, Zeeman splittings on the order of 5 MHz can be achieved [51], enabling frequency-selective addressing of magnetic sublevels. This feature is essential for techniques such as state initialization, selective shelving, and fine control of internal degrees of freedom. In addition, the 729 nm laser resolves the external motional modes in the trap. In the Lamb-Dicke regime, these are of the order of 1 MHz, enabling motional sidebands addressing. This feature is essential for techniques such as ground-state cooling, thermometry, and entanglement.

5.2 Coherent Addressing of the Electric Quadrupole Transition

In what follows, we will present the theoretical formalism of the quadrupole interaction, the selection rules, and how this transition is driven and observed in our experiment.

5.2.1 Electric Quadrupole Interaction

In many atomic systems, transitions between certain levels are forbidden under the electric dipole approximation due to symmetry or parity selection rules. In such cases, transitions can still occur via higher-order interactions. For the $4s^2S_{1/2} \leftrightarrow 3d^2D_{5/2}$ transition in $^{40}Ca^{+}$, the dominant contribution arises from the electric quadrupole interaction.

The interaction between the ion and the laser field can be expressed as [52]:

$$H_{E2}(t) = -e\,(\vec{\epsilon}\cdot\vec{r})\,(\vec{k}\cdot\vec{r})\,E_0\cos(\vec{k}\cdot\vec{r}-\omega t), \tag{46}$$

where $\vec{r}$ is the position operator of the electron, $\vec{\epsilon}$ and $\vec{k}$ are the polarization vector and the wavevector of the driving field, E_0 is its amplitude, e is the elementary charge, and ω is the radial frequency of the laser. This Hamiltonian captures the spatial variation of the laser field and its projection onto the atomic quadrupole structure. The product of the two scalar terms $(\vec{\epsilon}\cdot\vec{r})(\vec{k}\cdot\vec{r})$ reflects the second-order nature of the coupling, in contrast to the linear dependence found in electric dipole transitions.

5.2.2 Rabi Frequency for the Quadrupole Transition

The Rabi frequency for a quadrupole transition (Eq. 46) is given by [51]:

$$\Omega_0 = \left|\frac{eE_0}{2\hbar}\,\langle S_{1/2},m|(\vec{\epsilon}\cdot\vec{r})(\vec{k}\cdot\vec{r})|D_{5/2},m'\rangle\right|. \tag{47}$$

The matrix element in the above equation can be evaluated by expressing the bilinear product of vector operators as a rank-2 spherical tensor. The matrix element becomes [52]:

$$\Omega_0 = \left|\frac{eE_0}{2\hbar}\,\langle S_{1/2}||r^2C^{(2)}||D_{5/2}\rangle\sum_{q=-2}^{2}\begin{pmatrix}\frac{1}{2} & 2 & \frac{5}{2}\\ -m & q & m'\end{pmatrix}c_{ij}^{(q)}\,\epsilon_i k_j\right|, \tag{48}$$

where:

- $\langle S_{1/2}||r^2C^{(2)}||D_{5/2}\rangle$ is the reduced matrix element of the quadrupole operator,
- The $3j$-symbol encodes angular momentum selection rules and is proportional to the more well-known Clebsch–Gordan coefficients,
- $c_{ij}^{(q)}$ are numerical coefficients converting Cartesian products to spherical tensor components,

- ϵ_i and k_j are Cartesian components of the polarization and propagation vectors, respectively.

This form shows how the Rabi frequency depends both on internal atomic structure and on the external laser geometry (polarization and direction). The angular dependence enters through the contraction $\epsilon_i k_j$, while the state-specific coupling is set by the reduced matrix element and the $3j$-symbol.

5.2.3 Selection Rules and Parity Considerations

The electric quadrupole operator transforms as a rank-2 spherical tensor and imposes specific selection rules on allowed transitions. For quadrupole transitions between total angular momentum eigenstates $|\gamma J m\rangle$ and $|\gamma' J' m'\rangle$, the following selection rules apply:

- $\Delta J = 0, \pm 1, \pm 2$, but transitions with $J = J' = 0$ are forbidden.
- The initial and final states must have the same parity.
- $\Delta m = 0, \pm 1, \pm 2$.

In the case of $^{40}Ca^{+}$, the quadrupole transition $^2S_{1/2} \rightarrow ^2 D_{5/2}$ satisfies these conditions:

- $J = \frac{1}{2} \rightarrow J' = \frac{5}{2}$ is allowed by angular momentum rules,
- Both S and D orbitals have even parity, consistent with quadrupole (even-parity) transitions,
- Ground state sublevels $m = \pm\frac{1}{2}$ can couple to multiple sublevels in the $^2D_{5/2}$ manifold ($m' = \pm\frac{1}{2}, \pm\frac{3}{2}, \pm\frac{5}{2}$) via $\Delta m = 0, \pm 1, \pm 2$.

5.2.4 Geometric Coupling Tensor - $\mathcal{G}_q^{(2)}(\theta, \phi)$

The angular dependence of the quadrupole transition is captured by the geometric factor $\mathcal{G}_q^{(2)}(\theta, \phi)$, which reflects the projection of the laser's electric field and wavevector onto the spherical tensor components of the quadrupole operator. This factor arises from the contraction:

$$\mathcal{G}_q^{(2)} = \sum_{i,j} c_{ij}^{(q)} \, \epsilon_i k_j, \tag{49}$$

where $\vec{\epsilon}$ is the laser polarization vector, $\vec{k}$ is the wavevector, and $c_{ij}^{(q)}$ project the dyadic product $\epsilon_i k_j$ onto rank-2 spherical tensor components (see, e.g., Ref. [52] appendix).

We define the quantization axis (the direction of the magnetic field $\vec{B}$) to lie along the $\hat{z}$ direction and the two angles describing the laser geometry:

- ϕ: angle between the laser wavevector $\vec{k}$ and $\vec{B}$, such that $\vec{k} = k(\sin(\phi), 0, \cos(\phi))$.
- θ: angle of the linear polarization vector $\vec{\epsilon}$, such that $\vec{\epsilon} = (\cos\theta\cos\phi, \sin\theta, -\cos\theta\sin\phi)$.

The resulting coupling strength $g^{(q)} = |\mathcal{G}_q^{(2)}|/|k|$ determines the ability of the laser to drive transitions with $\Delta m = q$. For linearly polarized light, using the definitions above, the following expressions hold (see Fig. 11):

$$g^{(0)} = \frac{1}{2} \left| \cos\theta \, \sin(2\phi) \right|, \tag{50}$$

$$g^{(\pm 1)} = \frac{1}{\sqrt{6}} \left| \cos\theta \, \cos(2\phi) + i \sin\theta \cos\phi \right|, \tag{51}$$

$$g^{(\pm 2)} = \frac{1}{\sqrt{6}} \left| \frac{1}{2} \cos\theta \, \sin(2\phi) + i \sin\theta \sin\phi \right|. \tag{52}$$

These components describe the angular dependence of the laser-ion coupling strength for various Δm transitions, and allow for the design of laser geometries that maximize or suppress specific transitions. By selecting specific values of θ and ϕ, the experimentalist can enhance desired Zeeman transitions or eliminate undesired ones. This geometric control is essential in precision quantum-logic operations, state initialization, and sideband cooling.

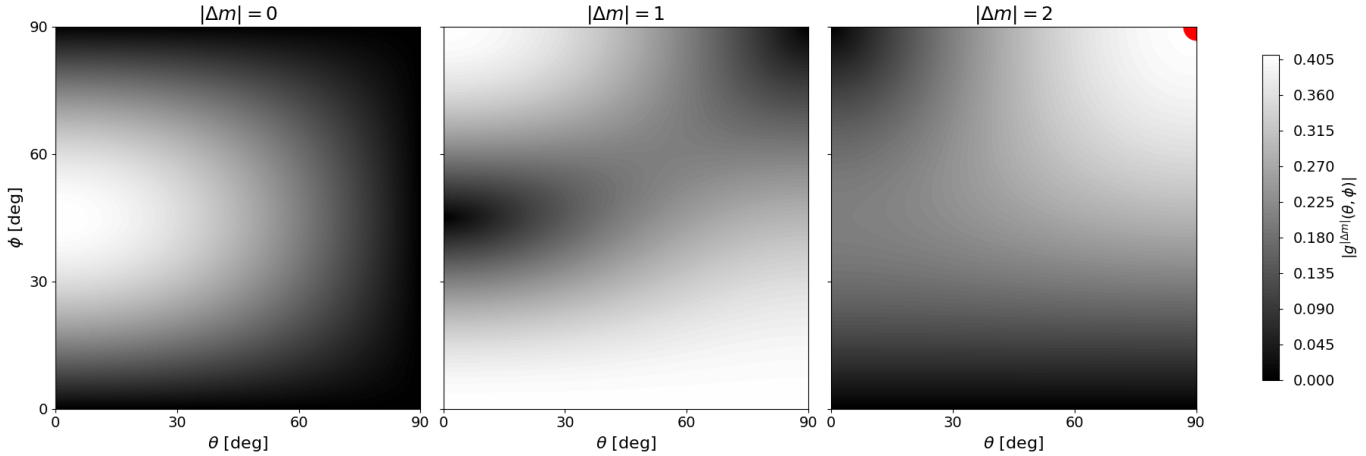

Figure 11: Angular dependence of the quadrupole coupling strength for $|\Delta m| = 0, 1, 2$. Shown are heatmap plots of $g^{(|\Delta m|)}(\theta, \phi)$ for linearly polarized light (Eqs. 50–52). Angles θ and ϕ are defined in the main text. The red region in the $|\Delta m| = 2$ panel highlights the geometry used in our experiment ($\theta = 90°$, $\phi = 90°$ - $\vec{B} \perp \vec{k} \perp \vec{\epsilon}$), which maximize coupling to the $\Delta m = \pm 2$ transitions while suppressing the remaining, $\Delta m = 0, \pm 1$ transitions.

5.2.5 Theoretical Estimate of the Rabi Frequency

As an example, we consider the quadrupole transition, ${}^2S_{1/2}\left(m = -\frac{1}{2}\right) \leftrightarrow {}^2D_{5/2}\left(m' = -\frac{5}{2}\right)$, in ${}^{40}Ca^+$. This transition satisfies $\Delta m = +2$, and we assume a laser geometry with $\theta = \phi = 90°$ (i.e., propagation and polarization both orthogonal to the magnetic field axis). In Table 1, we break Eq. 48 into its different components and give their numerical values. We use these to estimate the Rabi frequency under realistic lab conditions (see Appendix 8.3 for more details on the calculation). Our results demonstrate that Rabi π-pulses in the 5 μs range are achievable with moderate laser power and beam sizes.

Table 1: Experimental parameters and Rabi frequency estimate for the ${}^2S_{1/2}\,(m = -1/2) \leftrightarrow {}^2D_{5/2}\,(m = -5/2)$ quadrupole transition in ${}^{40}Ca^+$.

Parameter	**Value**
Transition frequency (f_0)	411042129776400.4 Hz [53]
Vacuum wavelength (λ_0)	729.3472767939427 nm
Laser power (P)	2 mW
Beam waist (w_0)	45 μm
Electric field amplitude ($E_0 = \sqrt{\frac{4P}{\pi\varepsilon_0 c w_0^2}}$)	2.18×10^4 V/m
Wavevector ($k = 2\pi/\lambda$)	8.61×10^6 m^{-1}
Reduced matrix element ($\mathrm{e}\langle S_{1/2} \left\| r^2 C^{(2)} \right\| D_{5/2}\rangle$)	9.733 ea_0^2 [54]
Wigner 3j ($\lvert\mathrm{Wj3}\rvert$)	$\sqrt{1/6}$
Geometric factor ($\lvert g^{(+2)}(90°, 90°)\rvert$)	$\sqrt{1/6}$
Calculated Rabi frequency ($\Omega_0/2\pi$)	103.0 kHz
π-pulse duration ($t_\pi = \pi/\Omega_0$)	4.85 μs

5.3 Zeeman Splitting in a Magnetic Field

In the presence of a weak external magnetic field **B**, the energy levels of the ion experience Zeeman splitting due to the interaction between the spin and angular momentum of the valence electron and the field. The first-order (linear) Zeeman shift for a fine-structure level $|J, m_J\rangle$ is given by [55]:

$$\Delta E = \mu_B g_J m_J B, \tag{53}$$

where:

- μ_B is the Bohr magneton,
- g_J is the Landé g-factor for the level,

- m_J is the magnetic quantum number,
- B is the magnitude of the magnetic field.

The Landé g-factor is computed as:

$$g_J \approx 1 + \frac{J(J+1) + S(S+1) - L(L+1)}{2J(J+1)}. \tag{54}$$

For the relevant states in $^{40}Ca^{+}$:

- $^2S_{1/2}$: $L = 0$, $S = 1/2$, $J = 1/2 \Rightarrow g_S \approx 2$,
- $^2D_{5/2}$: $L = 2$, $S = 1/2$, $J = 5/2 \Rightarrow g_D \approx \frac{6}{5}$.

Therefore, each magnetic sublevel, $|J, m_J\rangle$, shifts linearly with the field strength, and the transition frequencies between the $^2S_{1/2}$ and the $^2D_{5/2}$ levels split into ten distinct lines, depending on the combination of m_J and $m_{J'}$.

The frequency shift of each transition is:

$$\Delta f = \frac{1}{h}\mu_B B \left(g_D m_D - g_S m_S\right), \tag{55}$$

where g_S and g_D are the Landé factors for $S_{1/2}$ and $D_{5/2}$, respectively. These Zeeman patterns enable resolved addressing of individual quantum states and serves as a sensitive probe of the magnetic field in the location of the ion.

5.4 Rabi dynamics

When the frequency of the 729 nm laser is detuned close to resonance with one of the $^2S_{1/2} \leftrightarrow {}^2D_{5/2}$ transitions, the system exhibits a characteristic coherent two-level dynamics. The key parameters governing the behavior are the detuning $\Delta = \omega_{\text{laser}} - \omega_0$, the Rabi frequency Ω, and the pulse duration, t:

$$P_e(t) = \frac{\Omega^2}{\Omega^2 + \Delta^2} \sin^2\left(\frac{1}{2}\sqrt{\Omega^2 + \Delta^2}\, t\right). \tag{56}$$

The above expression shows that:

- The maximum excitation probability is reduced from unity to $\Omega^2/(\Omega^2 + \Delta^2)$.
- The Rabi oscillation frequency is increased to $\sqrt{\Omega^2 + \Delta^2}$.
- For large detunings ($|\Delta| \gg \Omega$), the population remains mostly in the ground state.

The excitation rate as a function of detuning defines the resonance line shape. For a driven two-level system, this is a Lorentzian [56]:

$$P_e(\Delta) \propto \frac{\Omega^2}{\Omega^2 + \Delta^2}. \tag{57}$$

5.4.1 Sideband Transitions and Rabi Dynamics in a Trapped-Ion System

In a trapped-ion system, the quantized motional modes of the ion couple to its internal electronic states. When driven by a narrow-linewidth laser on a quadrupole transition such as $S_{1/2} \leftrightarrow D_{5/2}$, the resulting excitation spectrum exhibits a central carrier line and motional sidebands spaced by integer multiples of the trapping mode's frequency, ω_{trap},

$$\omega_L = \omega_0 + k\,\omega_{\text{trap}}, \quad \text{with } k \in \mathbb{Z}.$$

These features are a direct consequence of the interaction between light and an harmonically-bound quantum system.

When the ion is initially in motional state n, the k-th sideband can drive transitions of the form:

$$|g, n\rangle \rightarrow |e, n + k\rangle.$$

In the more general case where the ion is in a thermal or mixed motional state, each sideband corresponds to a sum over many such transitions $|n_i\rangle \rightarrow |n_i + k\rangle$, each weighted by the initial state's population.

Lamb–Dicke Parameter: The strength of the coupling between motion and light is governed by the Lamb–Dicke parameter:

$$\eta = \frac{2\pi}{\lambda}\sqrt{\frac{\hbar}{2m\omega_{\text{trap}}}},$$

which represents the ratio of the ion's ground-state wavepacket size to the optical wavelength. When $\eta\bar{n} \ll 1$, where $\bar{n}$ is the mean motional occupation, the system is in the **Lamb–Dicke regime**, where sideband transitions can be treated perturbatively and the carrier transition dominates.

Rabi Frequencies: The Rabi frequencies for motional transitions in the Lamb–Dicke regime depend explicitly on the Lamb–Dicke parameter η and the motional quantum number n. They are given by:

- **Carrier transition** ($k = 0$):

  $$\Omega_{n,n} = \Omega_0\, e^{-\eta^2/2}\, L_n^0(\eta^2),$$

  where L_n^α is the generalized Laguerre polynomial. Expanding for $\eta \ll 1$, using $L_n^0(\eta^2) \approx 1 - n\eta^2$, we find:

  $$\Omega_{n,n} = \Omega_0 \left[1 - \frac{1}{2}\eta^2(2n+1) + \mathcal{O}(\eta^4)\right].$$

- **Red sideband** ($k = -1$):

  $$\Omega_{n,n-1} = \Omega_0\, e^{-\eta^2/2}\, \eta\, L_{n-1}^1(\eta^2)/\sqrt{n},$$

  which expands to (using $L_n^1(\eta^2) \approx (n+1)(1 - n\eta^2/2)$):

  $$\Omega_{n,n-1} = \eta\Omega_0\sqrt{n}\left[1 - \frac{1}{2}\eta^2 n + \mathcal{O}(\eta^4)\right].$$

- **Blue sideband** ($k = +1$):

  $$\Omega_{n,n+1} = \Omega_0\, e^{-\eta^2/2}\, \eta\, L_n^1(\eta^2)/\sqrt{n+1},$$

  which expands to:

  $$\Omega_{n,n+1} = \eta\Omega_0\sqrt{n+1}\left[1 - \frac{1}{2}\eta^2(n+1) + \mathcal{O}(\eta^4)\right].$$

These expressions capture the leading-order behavior in η, which is typically small in the Lamb–Dicke regime.

Transition Probability and Detuning Dependence: If the ion is in a non-Fock state with motional populations $\{p_n\}$, the total excitation probability is a weighted sum over contributions from each $n \to n+k$ transition (compare to Eq. 56):

$$P_e(t;\Delta_k) = \sum_{n=0}^{\infty} p_n\, \frac{\Omega_{n,n+k}^2}{\Omega_{n,n+k}^2 + \Delta_k^2}\sin^2\left(\frac{1}{2}\sqrt{\Omega_{n,n+k}^2 + \Delta_k^2}\, t\right),$$

where $\Omega_{n,n+k}$ is the Rabi frequency for the specific transition and $\Delta_k = \omega_L - (\omega_0 + k\omega_{\text{trap}})$ is the laser detuning from the k-th sideband. For a thermal distribution at mean occupation $\bar{n}$, the population of state n is [57]:

$$p_n = \frac{\bar{n}^n}{(1+\bar{n})^{n+1}}.$$

Applications: The sideband spectrum and its detuning-dependent lineshapes enable:

- Thermometry of the ion's motion via sideband amplitude asymmetry and Rabi thermometry on the carrier.
- Ground-state cooling by selectively driving red sidebands.
- Precise control of quantum logic gates through tailored Rabi dynamics.
- Spectroscopic determination of motional frequencies.

Understanding the full structure of sideband transitions and their Rabi dynamics is thus essential for high-fidelity quantum control in trapped-ion systems.

6 Results - Coherent Manipulation of the $^{40}Ca^{+}$ Quadrupole Transition

6.1 State Discrimination by Fluorescence Photon Counting

To determine whether the ion is in a bright ($|S\rangle$)or dark ($|D\rangle$) state , we measure the number of photons scattered during a fixed detection, $t_{\text{det}} = 1\,\text{ms}$, window while illuminating the ion with resonant 397 nm light. Photons are collected using a photomultiplier tube (PMT), and the signal is digitized as photon counts.

To calibrate the detection system and establish a reliable classification threshold, we acquire two reference histograms:

- **Bright histogram:** 397 nm and 866 nm lights on during detection, simulating the ion in a fluorescing, bright state.
- **Dark histogram:** 397 nm light on, however, 866 nm light off, simulating the absence of fluorescence - dark state.

Each condition is repeated 10,000 times, and the resulting photon counts are recorded. These two distributions are then used to define a threshold, T, that best separates bright and dark outcomes. For $n \geq T$, we classify the ion as bright, while for $n < T$ we classify the ion as dark.

Threshold Determination. We evaluate a range of candidate integer thresholds, T, and for each one we compute:

- The **Dark Error Fraction (DEF)**: fraction of dark events with $n \geq T$, misclassified as bright.
- The **Bright Error Fraction (BEF)**: fraction of bright events with $n < T$, misclassified as dark.

These rates are defined in terms of histogram counts:

$$\text{DEF}(T) = \frac{1}{N_{\text{dark}}} \sum_{n=T}^{\infty} D(n), \tag{58}$$

$$\text{BEF}(T) = \frac{1}{N_{\text{bright}}} \sum_{n=0}^{T-1} B(n), \tag{59}$$

where $D(n)$ and $B(n)$ are the photon count histograms for the dark and bright calibration runs, and N_{dark}, N_{bright} are the total number of events in each set.

The total classification error is then:

$$\text{Error}(T) = \text{DEF}(T) + \text{BEF}(T), \tag{60}$$

and the optimal threshold is chosen to minimize this error:

$$T_{\text{opt}} = \arg(\min_T[\,\text{Error}(T)]). \tag{61}$$

Figure 12 illustrates the result, we find the optimal threshold to be: $T_{\text{opt}} = 9$. The left panel shows the bright and dark photon count distributions. The right panel displays the dependence of error rates on the threshold value, with the optimal threshold clearly marked. We observe that with $t_{\text{det}} = 1\,\text{ms}$ we can achieve detection error smaller than 0.005.

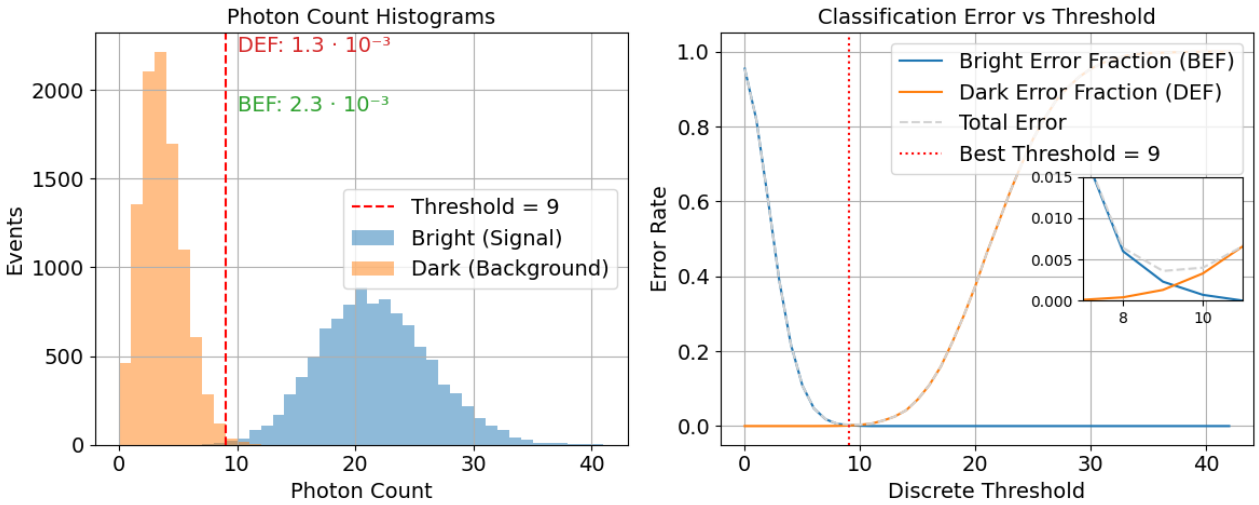

Figure 12: **Left:** Photon count histograms for bright (blue) and dark (orange) conditions, each based on 10,000 trials with detection window of $t_{\text{det}} = 1\,\text{ms}$. **Right:** bright error fraction (blue), dark error fraction (orange), and total classification error (gray dashed) as a function of threshold T. The optimal threshold ($T = 9$, red vertical line) minimizes the total error (< 0.005) and separates the two distributions.

6.2 729 nm Spectroscopy of the $^2S_{1/2} \rightarrow ^2D_{5/2}$ Transition

We have measured the spectrum of the electric quadrupole transition between the ground state, $^2S_{1/2}$, and the metastable state, $^2D_{5/2}$, in a trapped $^{40}Ca^+$ ion. The experimental sequence consists of three main phases: cooling, excitation, and detection. The ion is first Doppler cooled using 397 nm light (both near-resonance and red-detuned by ∼600 MHz), together with 866 nm light to repump population from the $D_{3/2}$ level. A brief 854 nm pulse is also applied to depopulate the long-lived $D_{5/2}$ state. After cooling, a 5 ms excitation pulse at 729 nm is applied to probe the narrow electric quadrupole transition. Detection follows immediately: both 397 nm and 866 nm beams are turned on, and fluorescence is collected via the PMT. The first millisecond records signal photons from the ion (either bright or dark depending on the spectroscopy), while the second millisecond measures the background level (dark ion) with the same detection beam configuration (866 laser is off). A technical error during this sequence resulted in an unintended activation of the red-detuned 397 nm beam during detection, which is marked in gray in Fig. 13.

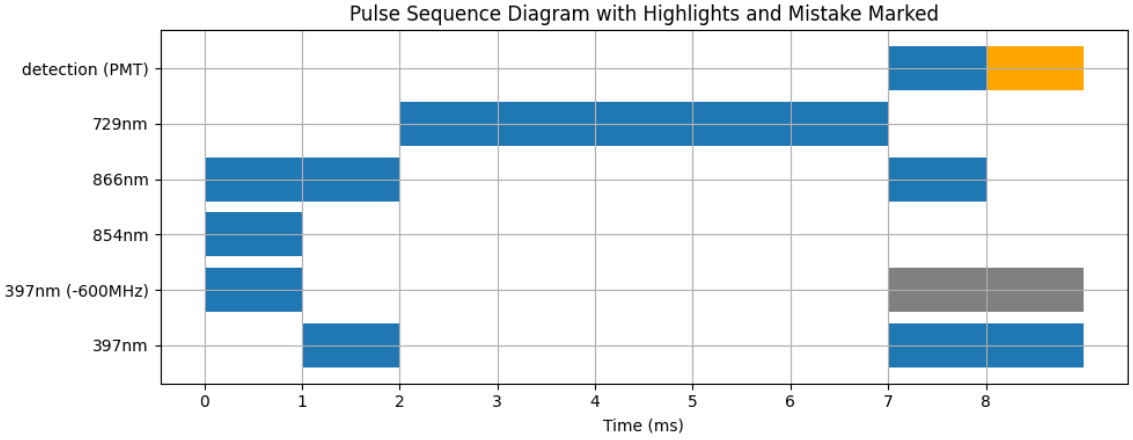

Figure 13: **Pulse sequence diagram for a single experimental cycle.** Each horizontal row represents a laser or detector channel, with time progressing from left to right in 1 ms bins. The first two milliseconds include Doppler cooling using 397 nm (red-detuned and near-resonant), 866 nm and an 854 nm repump and restart pulses. This is followed by a 5 ms excitation pulse at 729 nm targeting the qubit transition. The detection phase begins at 7 ms, where fluorescence from resonant 397 nm (866 nm is on) is counted using the PMT (blue bar). The final 1 ms (orange bar) measures background signal (397 nm is on but 866 nm is off). A mistakenly applied 397 nm (−600 MHz) pulse during detection is marked in gray.

Since we were not certain on the spatial alignment of the laser with the ion, we used a relatively long probe pulses ($t_{\text{pulse}} = 5\,\text{ms}$ instead of the estimated value - see Sec. 5.2.5). This long pulse enhances sensitivity to weak excitations and results in major decoherence effects (see Sec. 5.4.1) that leads to an approximately equal statistical population distribution between the S and D states. In addition, the ion's initial Zeeman substate was not prepared before each pulse. Assuming an equal statistical mixture of the $m_S = \pm 1/2$ Zeeman states, the maximum shelving probability is limited, under these conditions, to:

$$P_{\text{shelve,max}} \approx 0.5 \times 0.5 = 0.25. \tag{62}$$

Fig. 14 shows histograms of photon counts collected at two representative 729 frequency scan points. In the left panel, the laser was tuned to resonance, and two distinct populations are clearly observed: the bright state, corresponding to unshelved ions scattering photons, and the dark state, where the ion is shelved in the metastable $D_{5/2}$ level and only stray photon scattering are detected. In the right panel, the laser was detuned far from resonance, resulting in a single distribution consistent with bright-state detection. This contrast illustrates the efficiency of the shelving mechanism. The classification between bright and dark states was performed using a photon-count threshold of 9, as discussed in Sec. 6.1.

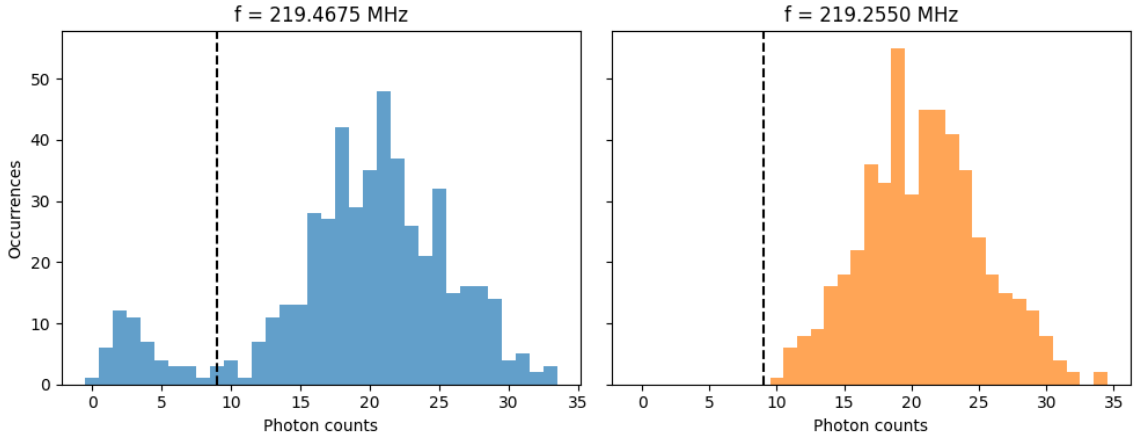

Figure 14: Photon-count histograms at two scan points: on-resonance (left) showing bright and dark populations, and off-resonance (right) showing only the bright distribution. The AOM frequency is given in the figure title. A threshold of 9 photons (black dashed line) was used to separate between the two states.

In Fig. 15, we present the measured excitation spectrum of the $S_{1/2} \rightarrow D_{5/2}$ transition. We observe a series of spectrally resolved peaks with Lorentzian-like envelopes. These peaks do not originate from Zeeman splitting. Instead, they result from motional sidebands induced by the ion-trap confinement. This effect will be discussed in detail in the next section.

The highest shelving probability achieved during these measurements was $P^{\text{max}}_{\text{shelve}} \approx \mathbf{0.125}$. The observed sub-maximal value suggests the presence of additional decoherence mechanisms, which we need to further investigate. Two main candidates are the way-to-long pulse time of 5 ms used in this experiment and the possibility of uneven statistical mixture in the two Zeeman sublevels of the $S_{1/2}$ state. Other possibilities include:

- Motion-induced decoherence due to imperfect cooling above the Doppler limit,
- Magnetic-field-induced decoherence,
- Laser phase or amplitude noise.

These effects degrade the excitation efficiency and spectral contrast, setting a practical resolution limit under the current experimental conditions.

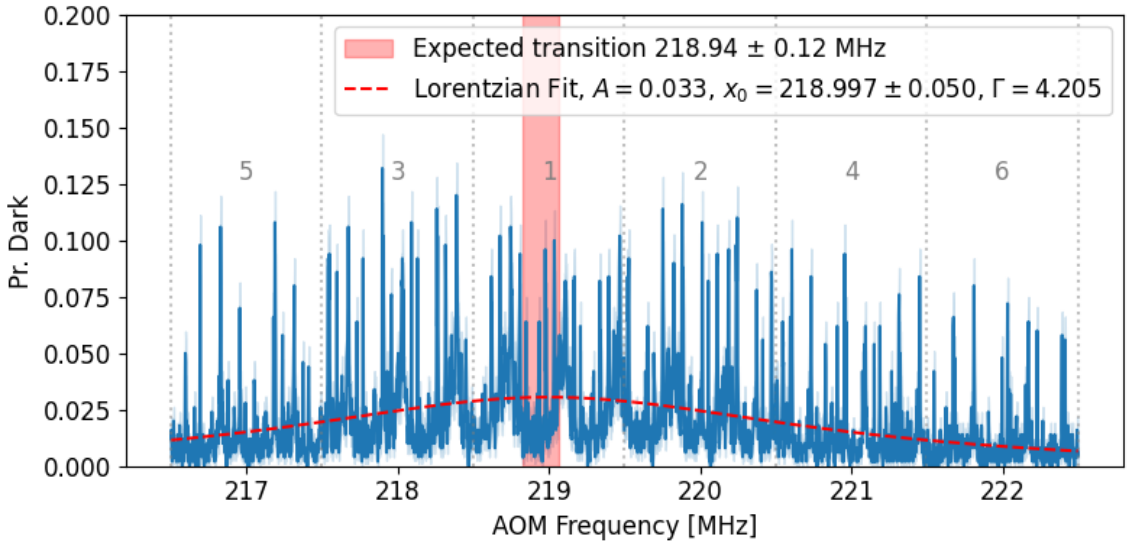

Figure 15: Measured excitation spectrum of the ${}^2S_{1/2} \rightarrow {}^2D_{5/2}$ transition in a single ${}^{40}Ca^+$ ion. The data is a composite of six sequential scans stitched together to span a wide frequency range. The horizontal axis shows the AOM drive frequency; due to the double-pass AOM configuration, the effective frequency shift applied to the laser is twice this value. The red shaded region denotes the expected AOM drive frequency for the $S_{1/2}(m_s = -1/2) \rightarrow D_{5/2}(m_d = -5/2)$ transition, calculated from a comb measurement and corrected for the Zeeman shift under the estimated magnetic field ($f_{\mathrm{AOM}} = 218.94 \pm 0.12\,\mathrm{MHz}$ - see Sec. 8.2). The vertical axis shows the shelving probability, obtained by thresholding photon counts at 9 counts (see Sec. 6.1). A Lorentzian envelope (dashed red curve) fitted to the peak structure yields a center frequency of $x_0 = 218.997 \pm 0.050\,\mathrm{MHz}$ and a full width at half maximum $\Gamma = 4.2\,\mathrm{MHz}$. The multiple peak structure within the envelope correspond to motional sidebands arising from the ion's secular motion in the trap.

6.2.1 Expected AOM Frequency for the $S_{1/2}(m_S = -1/2) \rightarrow D_{5/2}(m_D = -5/2)$ Transition

To guide the search for the quadrupole transition, we computed the expected AOM drive frequency for the $S_{1/2}(m_S = -1/2) \rightarrow D_{5/2}(m_D = -5/2)$ transition. This estimate combines our frequency comb measurement of the laser before the AOM with the known zero-field transition frequency and a correction for the Zeeman shift due to the applied magnetic field.

Because the AOM is operated in a double-pass configuration, the applied optical frequency shift is twice the AOM drive frequency. The measured optical offset and the calculated Zeeman correction (based on an estimated magnetic field and known Landé g-factors - see Sec. 5.3) yield a final estimate:

$$\boxed{f_{\mathrm{AOM}} = 218.941 \pm 0.119\ \mathrm{MHz}}. \tag{63}$$

A full derivation, including the uncertainty analysis from current fluctuations and mechanical coil tolerances, is provided in Appendix 8.2. While the estimation doesn't indicates one specific peak as the carrier transition, it does narrow down our potential candidates to only two. The discrepancy is most likely due to poor estimation of the real magnetic field in the ion position.

To identify characteristic periodic modulations in the spectral signal, we performed a discrete Fourier transform of the data. The resulting spectrum (shown in Fig. 16), plotted in inverse frequency units ($1/f$), reveals clear peaks corresponding to temporal oscillations. The most significant peak is located at $f = 733.4 \pm 40.1$ kHz, which is in good agreement with the independently measured axial frequency of the ion, $f_{\mathrm{tickle}} = 718.0 \pm 0.1$ kHz using the "tickle" method. The deviation between the two is only $\sim 0.38\ \sigma$, indicating that the repeating peaks in the spectrum are indeed motional sidebands. In addition to the dominant resonance, several smaller peaks appear at lower frequencies in the $1/f$ domain. These features likely reflect higher harmonics of the tarp resonance.

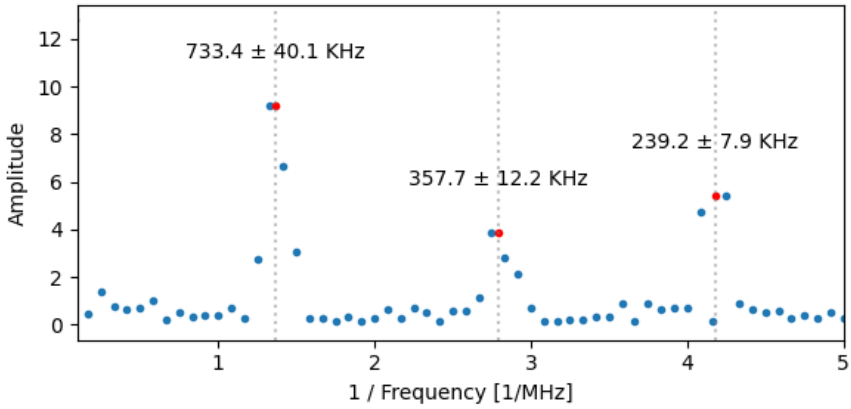

Figure 16: Discrete Fourier transform of the dark-state probability. The spectrum is plotted as a function of inverse frequency, $1/f$, such that peaks correspond to characteristic time-domain periodicities in the excitation signal. The labeled peaks correspond to the inverse of the detected frequencies and are annotated at the center of each locally fitted Gaussian. Red dots mark the maxima of these Gaussian fits, and the quoted uncertainties are derived from their fitted widths. The most prominent resonance occurs at 733.4 ± 40.1 kHz, with additional weaker components observed at 357.7 ± 12.2 kHz and 239.2 ± 7.9 kHz, that can correspond to the second and third harmonics accordingly.

7 Discussion

This work demonstrates that laser-frequency stabilization based on injection locking and fiber-noise cancellation can provide the spectral resolution needed to interrogate the narrow electric quadrupole transition in a single trapped $^{40}Ca^{+}$ ion. The system resolves Zeeman substructure and motional sidebands of the $^2S_{1/2}(m = -1/2) \leftrightarrow {}^2D_{5/2}(m = -5/2)$ transition, suggesting that the phase stability of the laser and its delivery path meet the requirements for coherent spectroscopy.

The main objective of this thesis was to implement a 729 nm laser system capable of addressing a single ion with high spectral precision. Injection locking enabled robust frequency lock of a diode laser, and the addition of an active fiber-noise-cancellation (FNC) loop suppressed environmentally induced phase fluctuations over the 120 m delivery fiber. The performance of the PLL was verified using out-of-loop measurements of the phase noise power spectral density, which showed significant suppression up to ~ 2 kHz.

In parallel, we characterized the injection locking behavior across various diode current and temperature settings, as well as injected power. The observed relation between diode current and internal temperature and locking range as a function of injected power confirmed the expected thermal tuning behavior. This characterization supports reliable injection locking by offering a predictive map of laser behavior across operating conditions. The consistency of this relation adds a practical tool for future automated or feedback-based tuning schemes.

These results support the initial hypothesis that the combination of injection locking and active phase noise cancellation is sufficient for high-resolution spectroscopy in trapped-ion systems. While we do not directly compare our system to cavity- or comb-stabilized references, the measured linewidth and observed spectrum are consistent with what is expected for such systems, and are compatible with the level of stability required for spectroscopy-driven ion state control.

Future Developments. Much like Moses, who led his people to the edge of the Promised Land but did not enter it himself, this thesis brings us to the threshold of a vast and exciting landscape of possibilities, though it does not venture fully into them. The work presented here demonstrates that our system functions reliably and can serve as a robust platform. However, this is merely the beginning. Having established the core tools—namely, a stable and coherent laser system, effective state detection, and reliable ion control—we are now equipped to explore more advanced applications. These include performing precision spectroscopy on a single ion, ground-state cooling, and implementing quantum logic spectroscopy in conjunction with molecular ions. Each of these avenues holds the potential for impactful scientific contributions, and they all stem from the foundation laid in this work.

References

[1] M. A. Lombardi, T. P. Heavner, and S. R. Jefferts, "NIST primary frequency standards and the realization of the si second", NCSLI Measure **2**, 74–89 (2007).

[2] J. I. Cirac and P. Zoller, "Quantum computations with cold trapped ions", Phys. Rev. Lett. **74**, 4091–4094 (1995).

[3] N. Dimarcq et al., "Roadmap towards the redefinition of the second", Metrologia **61**, 10.1088/1681-7575/ad17d2 (2024).

[4] C. R. Monroe and D. J. Wineland, "Quantum computing with ions", Scientific American **299**, 64–71 (2008).

[5] A. L. Schawlow and C. H. Townes, "Infrared and optical masers", Phys. Rev. **112**, 1940–1949 (1958).

[6] C. Hagemann, C. Grebing, C. Lisdat, S. Falke, T. Legero, U. Sterr, F. Riehle, M. J. Martin, and J. Ye, "Ultrastable laser with average fractional frequency drift rate below 5× 10- 19/s", Optics letters **39**, 5102–5105 (2014).

[7] T. Kessler, C. Hagemann, C. Grebing, T. Legero, U. Sterr, F. Riehle, M. Martin, L. Chen, and J. Ye, "A sub-40-mHz-linewidth laser based on a silicon single-crystal optical cavity", Nature Photonics **6**, 687–692 (2012).

[8] T. Manovitz, Y. Shapira, L. Gazit, N. Akerman, and R. Ozeri, "Trapped-ion quantum computer with robust entangling gates and quantum coherent feedback", PRX Quantum **3**, 010347 (2022).

[9] M. C. Marshall et al., "High-Stability Single-Ion Clock with 5.5×10^{-19} Systematic Uncertainty", arXiv:2504.13071 [physics.atom-ph] (2025).

[10] A. Aeppli, K. Kim, W. Warfield, M. S. Safronova, and J. Ye, "Clock with 8×10^{-19} systematic uncertainty", Phys. Rev. Lett. **133**, 023401 (2024).

[11] S. Lee, G. Moon, S. E. Park, H.-G. Hong, J. H. Lee, S. Seo, T. Y. Kwon, and S.-B. Lee, "Laser frequency stabilization in the 10 −14 range via optimized modulation transfer spectroscopy on the 87Rb D2 line", Opt. Lett. **48**, 1020–1023 (2023).

[12] R. Santra, E. Arimondo, T. Ido, C. H. Greene, and J. Ye, "High-accuracy optical clock via three-level coherence in neutral bosonic Sr 88", Physical Review Letters **94**, 173002 (2005).

[13] U. Schünemann, H. Engler, R. Grimm, M. Weidemüller, and M. Zielonkowski, "Simple scheme for tunable frequency offset locking of two lasers", Review of Scientific Instruments **70**, 242–243 (1999).

[14] D. Leibfried, R. Blatt, C. Monroe, and D. Wineland, "Quantum dynamics of single trapped ions", Rev. Mod. Phys. **75**, 281–324 (2003).

[15] C. Chou, A. L. Collopy, C. Kurz, Y. Lin, M. E. Harding, P. N. Plessow, T. Fortier, S. Diddams, D. Leibfried, and D. R. Leibrandt, "Frequency-comb spectroscopy on pure quantum states of a single molecular ion", Science **367**, 1458–1461 (2020).

[16] S. Patra, M. Germann, J.-P. Karr, M. Haidar, L. Hilico, V. Korobov, F. Cozijn, K. Eikema, W. Ubachs, and J. Koelemeij, "Proton-electron mass ratio from laser spectroscopy of HD+ at the part-per-trillion level", Science **369**, 1238–1241 (2020).

[17] M. Safronova, D. Budker, D. DeMille, D. F. J. Kimball, A. Derevianko, and C. W. Clark, "Search for new physics with atoms and molecules", Reviews of Modern Physics **90**, 025008 (2018).

[18] P. Spano, S. Piazzolla, and M. Tamburrini, "Frequency and intensity noise in injection-locked semiconductor lasers: theory and experiments", IEEE Journal of Quantum Electronics **QE-22**, 421–434 (1986).

[19] B. P. Dix-Matthews, S. W. Schediwy, D. R. Gozzard, E. Savalle, F.-X. Esnault, T. Lévèque, C. Gravestock, D. D'Mello, S. Karpathakis, M. Tobar, et al., "Point-to-point stabilized optical frequency transfer with active optics", Nature communications **12**, 515 (2021).

[20] S. M. McSorley, B. P. Dix-Matthews, A. M. Frost, A. S. McCann, S. F. Karpathakis, D. R. Gozzard, S. M. Walsh, and S. W. Schediwy, "Free-space optical-frequency comparison over rapidly moving links", Phys. Rev. Appl. **23**, L021003 (2025).

[21] O. Lib, G. Hasson, and Y. Bromberg, "Real-time shaping of entangled photons by classical control and feedback", Science Advances **6**, eabb6298 (2020).

[22] D. P. Greenwood and C. A. Primmerman, "Adaptive optics research", Lincoln Laboratory Journal **5** (1992).

[23] T. Levin and Z. Meir, "Coherent dynamics of a nuclear-spin-isomer superposition", Phys. Rev. Res. **7**, 013274 (2025).

[24] E. Madge, G. Perez, and Z. Meir, "Prospects of nuclear-coupled-dark-matter detection via correlation spectroscopy of I_2^+ and Ca^+", Phys. Rev. D **110**, 015008 (2024).

[25] D. F. Jackson Kimball and K. Van Bibber, *The search for ultralight bosonic dark matter* (Springer Nature, 2023).

[26] R. Adler, "A study of locking phenomena in oscillators", Proc. IRE **34**, 351–357 (1946).

[27] H. L. Stover and W. H. Steier, "Locking of laser oscillators by light injection", Appl. Phys. Lett. **8**, 91–93 (1966).

[28] K. Shimoda, "Theory of laser oscillation", in *Introduction to laser physics*, Vol. 44, Springer Series in Optical Sciences (Springer, Berlin, Heidelberg, 1984), pp. 179–215.

[29] R. Lang, "Injection locking properties of a semiconductor laser", IEEE J. Quantum Electron. **18**, 976–983 (1982).

[30] J. Liu et al., "Optical injection locking: from principle to applications", J. Lightwave Technol. **37**, 643–655 (2019).

[31] Y. P. Varshni, "Temperature dependence of the energy gap in semiconductors", physica **34**, 149–154 (1967).

[32] H. Y. Fan, "Energy gap in semiconductors at high temperatures", Physical Review **82**, 900 (1951).

[33] T. Oyama and S. Muto, "Theory of energy gap temperature dependence", Progress of Theoretical Physics **5**, 833 (1950).

[34] S. Antoncik, "Energy gap shift at high temperatures", Czech Journal of Physics **5**, 449 (1955).

[35] Y. A. Goldberg and N. M. Shmidt, "GALLIUM INDIUM ARSENIDE PHOSPHIDE ($Ga_xIn_{1-x}AS_yP_{1-y}$)", in *Handbook series on semiconductor parameters* (1999) Chap. 7, pp. 153–179.

[36] O. Lopez, A. Haboucha, B. Chanteau, C. Chardonnet, A. Amy-Klein, and G. Santarelli, "Ultra-stable long-distance optical frequency distribution using the internet fiber network", Optics Express **20**, 23518–23526 (2012).

[37] P. A. Williams, W. C. Swann, and N. R. Newbury, "High stability transfer of an optical frequency over long fiber-optic links", Optica **25**, 1284–1293 (2008).

[38] E. Benkler, C. Lisdat, and U. Sterr, "On the relation between uncertainties of weighted frequency averages and the various types of allan deviation", Metrologia **52**, 565–574 (2015).

[39] M. Alon, N. Akerman, E. Shafir, and R. Ozeri, "Frequency dissemination with less than 2×10^{-18} fractional-frequency instability over 120 km of a commercial fiber infrastructure", in European frequency and time forum (eftf) (2024), pp. 274–276.

[40] E. Rubiola and F. Vernotte, "The Companion of Enrico's Chart for Phase Noise and Two-Sample Variances", IEEE Transactions on Microwave Theory and Techniques **71**, 2996–3025 (2023).

[41] G. Di Domenico, S. Schilt, and P. Thomann, "Simple approach to the relation between laser frequency noise and laser line shape", Applied Optics **49**, 4801–4807 (2010).

[42] A. Kreuter et al., "Experimental and theoretical study of the $3d\ ^2D$–level lifetimes of $^{40}Ca^+$", Phys. Rev. A **71**, 032504 (2005).

[43] P. Barakhshan, A. Marrs, A. Bhosale, B. Arora, R. Eigenmann, and M. S. Safronova, *Portal for High-Precision Atomic Data and Computation(version 2.0).* Feb. 2022.

[44] H. C. Nägerl, C. Roos, H. Rohde, D. Leibfried, J. Eschner, F. Schmidt-Kaler, and R. Blatt, "Single ions in paul traps", in Decoherence: theoretical, experimental, and conceptual problems, edited by P. Blanchard, E. Joos, D. Giulini, C. Kiefer, and I.-O. Stamatescu (2000), pp. 213–231.

[45] J. Shang, J. Cao, K. Cui, S. Wang, P. Zhang, J. Yuan, S. Chao, H. Shu, and X. Huang, "A compact, sub-Hertz linewidth 729 nm laser for a miniaturized $^{40}Ca^{+}$ optical clock", Optics Communications **382**, 410–414 (2017).

[46] H. Häffner et al., "Scalable multiparticle entanglement of trapped ions", Appl. Phys. B **81**, 151–153 (2005).

[47] P. O. Schmidt, T. Rosenband, C. Langer, W. M. Itano, J. C. Bergquist, and D. J. Wineland, "Spectroscopy using quantum logic", Science **309**, 749–752 (2005).

[48] N. Akerman, N. Navon, S. Kotler, Y. Glickman, and R. Ozeri, "Universal gate-set for trapped-ion qubits using a narrow linewidth diode laser", New Journal of Physics **17**, 113060 (2015).

[49] E. C. Reed, L. Qi, and K. R. Brown, "Comparison of continuous and pulsed sideband cooling on an electric quadrupole transition", Physical Review A **110**, 013123 (2024).

[50] A. Kramida, Yu. Ralchenko, Reader, J., and and NIST ASD Team, *NIST Atomic Spectra Database (ver. 5.10)*, National Institute of Standards and Technology, Gaithersburg, MD, 2022.

[51] C. Roos, *Controlling the quantum state of trapped ions*, 2000.

[52] D. F. V. James, "Quantum dynamics of cold trapped ions with application to quantum computation", Applied Physics B **66**, 181–190 (1998).

[53] H. S. Margolis, G. Panfilo, G. Petit, C. Oates, T. Ido, and S. Bize, "The CIPM list 'Recommended values of standard frequencies': 2021 update", Metrologia **61**, 035005 (2024).

[54] H. Shao, Y. Huang, H. Guan, C. Li, T. Shi, and K. Gao, "Precise determination of the quadrupole transition matrix element of $^{40}Ca^{+}$ via branching-fraction and lifetime measurements", Phys. Rev. A **95**, 053415 (2017).

[55] C. J. Foot, *Atomic physics*, Vol. 7 (Oxford university press, 2005).

[56] R. Loudon, *The quantum theory of light* (OUP Oxford, 2000).

[57] D. J. Wineland, C. Monroe, W. M. Itano, D. Leibfried, B. E. King, and D. M. Meekhof, "Experimental issues in coherent quantum-state manipulation of trapped atomic ions", J. Res. Natl. Inst. Stan. **103**, 259 (1998).

8 Appendix

8.1 Diode $I - V$ relation

8.1.1 Extraction of I_0 from the Diode Equation

Below the threshold current, the current-voltage relationship of a diode follows the well-known diode equation:

$$I = I_0 \left(e^{V/V_T} - 1 \right), \tag{64}$$

where:

- I_0 is the reverse current,
- $V_T = \frac{nk_BT}{q}$ is the thermal voltage ($\approx n25.8$ mV at room temperature, with n an empirical coefficient),
- V is the applied voltage across the diode.

For very low currents ($I \ll I_{\text{th}}$), the diode operates in the subthreshold region before lasing begins. By measuring the $I - V$ curve in this regime, we determine I_0 experimentally by (see Fig. 17):

1. Measure the $I - V$ curve in the subthreshold region (before lasing).
2. Fit the exponential region using:

$$\ln I = \ln I_0 + \frac{V}{V_T}.$$

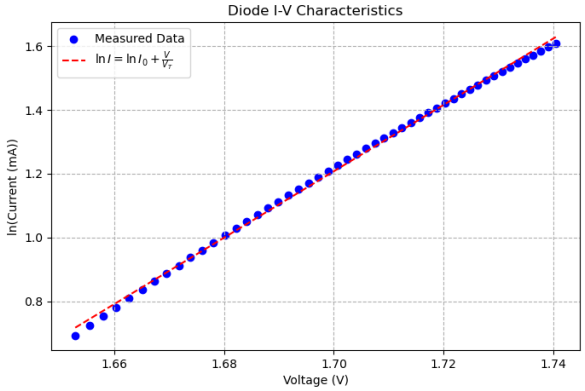

Figure 17: Laser-diode ($I - V$) curve at $I \ll I_{th}$. Blue dots are measured diode current vs diode voltage, red-dashed line is a linear fit (see text) from which we extract $I_0 = 98.4\,\text{nA}$ and $V_T = 113\,\text{mV}$.

8.1.2 Voltage Saturation in Laser Diodes

Above the lasing threshold current I_{th}, the voltage across a laser diode exhibits saturation behavior, deviating from the exponential increase observed in conventional p-n junction diodes. In this regime, the total current can be approximated as:

$$I = I_{\text{th}} + \frac{V - V_{\text{th}}}{R_s} + I_{\text{stim}}, \tag{65}$$

where:

- V_{th} is the threshold voltage,
- R_s is the series resistance,
- I_{stim} is the stimulated recombination current contributing to optical power,

and accordingly:

$$V = R_s I + V_0. \tag{66}$$

Since above threshold the majority of carriers contribute to stimulated emission rather than increasing the junction voltage, V increases only slowly with current. The measured $V - I$ characteristics in this region confirm that differential resistance (dV/dI) decreases significantly, leading to a flattened voltage response (see Fig. 18).

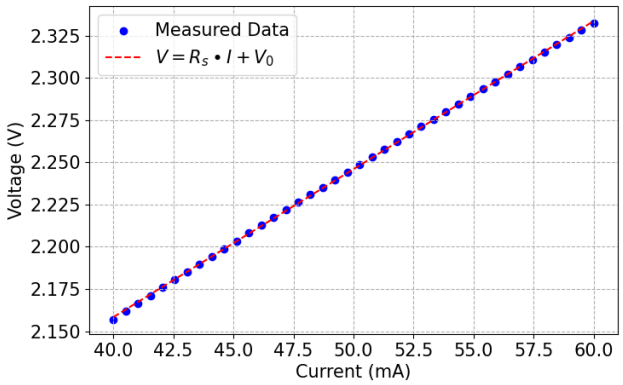

Figure 18: Laser-diode ($V - I$) curve at $I > I_{th}$. Blue dots are measured voltage vs. current characteristics above threshold, red dashed line is a linear fit (see text) from which we extract, $R_s = 8.76\,\Omega$hm, and $V_0 = 1.8\,$V.

This effect is essential in thermal management and laser diode efficiency, as it limits excess electrical power dissipation while ensuring a stable optical output.

8.2 Calculation of Zeeman Shift and AOM Frequency Uncertainty

To determine the expected AOM drive frequency for the $S_{1/2}(m_s = -1/2) \rightarrow D_{5/2}(m_d = -5/2)$ transition, we begin from the known optical frequency offset measured with the frequency comb:

$$\Delta f = f_{\text{meas}} - f_0 = -445{,}358{,}937 \text{ Hz}, \tag{67}$$

where f_0 is the zero-field transition frequency and f_{meas} is the comb-measured frequency after the fiber noise cancellation (FNC) stage.

The AOM is operated in a double-pass configuration. Therefore, the required AOM drive frequency (half the total frequency shift) is:

$$f_{\text{AOM}}^{(0)} = \frac{|\Delta f|}{2} = 222.679 \text{ MHz}. \tag{68}$$

Zeeman-Shift Correction

We apply a first-order Zeeman correction to account for the magnetic field:

$$\Delta f_{\text{Zeeman}} = \mu_B B(g_D m_D - g_S m_S), \tag{69}$$

with:

$$\begin{aligned} \mu_B &= 1.3996 \text{ MHz/G}, \\ g_D &= 1.2003, & m_D &= -\tfrac{5}{2}, \\ g_S &= 2.0023, & m_S &= -\tfrac{1}{2}, \\ B &= 1.95 \text{ A} \times 1.37 \text{ G/A} = 2.67 \text{ G}. \end{aligned}$$

The magnetic-field coils response of 1.37 G/A was calculated based on the work of Oz Matoki in his summer rotation project.

Evaluating:

$$\Delta(gm) = g_D m_D - g_S m_S = -3.00075 + 1.00115 = -1.9996, \tag{70}$$

$$\Delta f_{\text{Zeeman}} = \mu_B \cdot B \cdot \Delta(gm) = 1.3996 \cdot 2.67 \cdot (-1.9996) \approx -7.48 \text{ MHz}. \tag{71}$$

Thus, the corrected expected AOM frequency is:

$$f_{\text{AOM}} = f_{\text{AOM}}^{(0)} + \Delta f_{\text{Zeeman}}/2 = 222.679 - 7.48/2 = \boxed{218.941 \text{ MHz}}. \tag{72}$$

Uncertainty Estimate

We now estimate the uncertainty in the AOM frequency due to uncertainties in the value of the magnetic field in the trap.

Sources of Uncertainty:

- Mechanical tolerance in coil placement: $\Delta R = \pm 3$ mm.
- Current source fluctuations: $\Delta I = \pm 0.03$ A.

Magnetic Field Uncertainty: The current-to-field conversion is 1.37 G/A, giving:

$$\delta B_{\text{mech}} \approx \pm 0.075 \text{ G}, \tag{73}$$

$$\delta B_{\text{curr}} = 1.37 \cdot 0.03 = 0.0411 \text{ G}, \tag{74}$$

$$\delta B = \sqrt{(0.075)^2 + (0.0411)^2} \approx \boxed{0.085 \text{ G}}. \tag{75}$$

Propagation to AOM Frequency:

$$\delta f_{\text{AOM}} = \frac{\mu_B \cdot \delta B \cdot |\Delta(gm)|}{2} = \frac{1.3996 \cdot 0.085 \cdot 1.9996}{2} \approx \boxed{119 \text{ kHz}}. \tag{76}$$

Final Result: The expected AOM drive frequency for the desired transition is therefore:

$$\boxed{f_{\text{AOM}} = 218.941 \pm 0.119 \text{ MHz}}. \tag{77}$$

8.3 Rabi Frequency Calculation for the Quadrupole Transition

We calculate the Rabi frequency for the electric quadrupole transition,

$$^2S_{1/2}(m_J = -1/2) \leftrightarrow {}^2D_{5/2}(m_J = -5/2),$$

driven by a 729 nm laser beam of power, P, and waist, w_0, under a geometry where the polarization and wavevector are both orthogonal to the quantization axis ($\theta = \phi = 90°$).

We can rewrite Eq. 48 from the main text as

$$\Omega = \left| \frac{E_0 k}{2\hbar} \cdot e\langle S_{1/2} \left\| r^2 C^{(2)} \right\| D_{5/2} \rangle \cdot |\text{Wj3}| \cdot |g^{(q)}(\theta, \phi)| \right|,$$

where:

- $E_0 = \sqrt{\frac{4P}{\pi \varepsilon_0 c w_0^2}}$ is the electric field amplitude,
- $k = \frac{2\pi}{\lambda}$ is the wavevector,
- $e\langle S_{1/2} \| r^2 C^{(2)} \| D_{5/2} \rangle = 9.733\, e a_0^2$ is the reduced matrix element [54],
- $|\text{Wj3}| = \sqrt{1/6}$ is the Wigner 3j coefficient,
- $|g^{(2)}(\theta = 90°, \phi = 90°)| = \sqrt{1/6}$ is the angular factor for this geometry.

We use the following parameters in the calculation:

$$
\begin{aligned}
P &= 2\ \text{mW}, & w_0 &= 45\ \mu\text{m},\\
\lambda &= 729.347276793942\ \text{nm}, & \varepsilon_0 &= 8.8541878188(14) \times 10^{-12}\ \text{F/m},\\
c &= 299,792,458\ \text{m/s}, & \hbar &= 1.05457182 \times 10^{-34}\ \text{J·s},\\
e &= 1.60217663 \times 10^{-19}\ \text{C}, & a_0 &= 5.29177210544(82) \times 10^{-11}\ \text{m}.
\end{aligned}
$$

From these values, we compute:

$$
\begin{aligned}
E_0 &= 2.18 \times 10^4\ \text{V/m},\\
k &= 8.61 \times 10^6\ \text{m}^{-1},\\
e\langle S_{1/2} \| r^2 C^{(2)} \| D_{5/2} \rangle &= 4.36 \times 10^{-39}\ \text{C·m}^2,\\
\Omega/2\pi &\approx \boxed{103.0\ \text{kHz}},\\
t_\pi &= \boxed{4.85\ \mu\text{s}}.
\end{aligned}
$$

This result is consistent with experimentally measured π-pulse durations on the ${}^2S_{1/2} \leftrightarrow {}^2D_{5/2}$ transition in trapped ${}^{40}\text{Ca}^+$ ions.